

NASA Technical Memorandum 4441

IN-02
163194
P.50

Assessment of a Flow-Through Balance for Hypersonic Wind Tunnel Models With Scramjet Exhaust Flow Simulation

Lawrence D. Huebner, Marc W. Kniskern,
and William J. Monta

MAY 1993

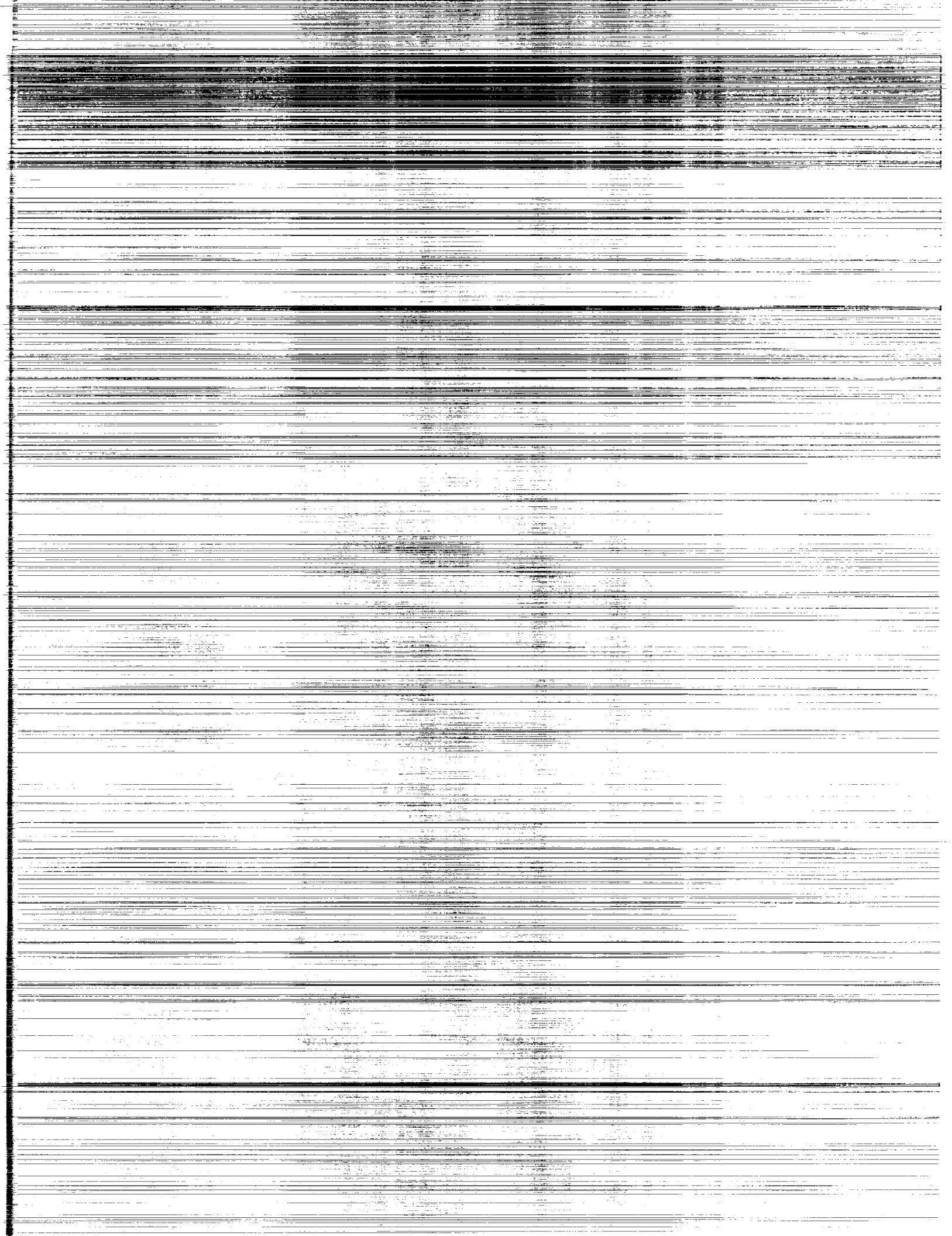
(NASA-TM-4441) ASSESSMENT OF A
FLOW-THROUGH BALANCE FOR HYPERSONIC
WIND TUNNEL MODELS WITH SCRAMJET
EXHAUST FLOW SIMULATION (NASA)
50 p

N93-27005

Unclas

H1/02 0163194

NASA



Assessment of a Flow-Through Balance for Hypersonic Wind Tunnel Models With Scramjet Exhaust Flow Simulation

Lawrence D. Huebner
Langley Research Center
Hampton, Virginia

Marc W. Kniskern
North Carolina State University
Raleigh, North Carolina

William J. Monta
Langley Research Center
Hampton, Virginia



National Aeronautics and
Space Administration
Office of Management
Scientific and Technical
Information Program

1993

The use of trademarks or names of manufacturers in this report is for accurate reporting and does not constitute an official endorsement, either expressed or implied, of such products or manufacturers by the National Aeronautics and Space Administration.

Summary

Thermal effects have been assessed on a non-watercooled, flow-through balance with exhaust gas simulation and external aerodynamic heating. The purposes of this investigation were twofold: first, to determine whether accurate force and moment data could be obtained during hypersonic wind tunnel tests of a model with a scramjet exhaust flow simulation that employs a representative non-watercooled, flow-through balance; second, to analyze temperature time histories on various parts of the balance to address thermal effects on force and moment data. A stainless steel model of a hypersonic, airbreathing-propulsion cruise missile concept (HAPCM-50) was used to evaluate this balance. The tests were conducted in the NASA Langley Research Center 20-Inch Mach 6 Wind Tunnel at free-stream Reynolds numbers of 0.5 to $7.4 \times 10^6/\text{ft}$ and at nominal angles of attack of -3.5° , 0° , and 5° . The simulant exhaust gases included cold air, hot air, and a mixture of 50 percent each by volume of Argon and Freon (Ar-Fr) and reached stagnation temperatures within the balance of 111° , 214° , and 283°F , respectively. Throughout the tests on this model, normal and side forces as well as yawing, rolling, and pitching moments were unaffected by the balance thermal response from the simulant gases and the high-temperature wind tunnel flow. However, the axial-force measurements were significantly affected by balance heating; the average zero shifts in these measurements were 2.1, 4.6, and 6.4 percent of full scale for the cold-air, hot-air, and Ar-Fr exhaust simulations, respectively. This investigation showed that for this model at the conditions tested, a nonwatercooled, flow-through balance is not suitable for axial-force measurements during scramjet exhaust flow simulation tests at hypersonic speeds. In general, a heated exhaust gas may produce unacceptable force and moment uncertainties when used with thermally sensitive balances. However, the axial-force shifts may be reduced if the forward and aft sections of the axial-force bridge circuit are calibrated independently.

Introduction

The current renewed interest in hypersonic airbreathing vehicles such as the National Aero-Space Plane (NASP) has focused attention on the accuracy and suitability of hypersonic test methods for assessing aerodynamic performance of this class of vehicles. Wind tunnel tests of entire hypersonic-vehicle configurations that employ supersonic combustion ramjet (scramjet) engine simulation are of particular interest. Scramjet engine simulation is essential for

evaluations of the powered aerodynamic performance because the entire underside surface of these vehicles is highly integrated with the propulsion system. Specifically, the forebody surface compresses the flow before it reaches the inlet, and the aftbody surface is an extension of the nozzle to expand the flow and to provide for maximum thrust and pitching-moment trim (ref. 1). A primary hypersonic aerodynamic performance parameter for this class of vehicles is the difference between vehicle thrust and drag forces. Therefore, accurate measurement of the axial force is critical to estimations of aerodynamic performance.

However, duplication of scramjet engine operation is not feasible for wind tunnel models because the combustion process is not geometrically scalable and the high stagnation pressures and temperatures necessary to sustain combustion are difficult to obtain in existing wind tunnels (ref. 2). The dilemma posed by the need for simulating scramjet engine operation and the impracticality of scaling a scramjet combustor has led to the use of a substitute cold (non-combusting) gas to simulate the scramjet exhaust. (See ref. 3.) This technique is acceptable for matching the desired pressure distribution over the external nozzle; thus, scramjet engine effects upon vehicle aerodynamic forces and moments are well simulated.

Under the direction of NASA Langley Research Center, a survey was conducted to determine potentially suitable methods for obtaining aerodynamic data on hypersonic wind tunnel models with scramjet exhaust flow simulation (ref. 2). The most effective method involves a flow-through, strain gauge force balance that provides a passage within the model for the simulant scramjet exhaust gas. Based on this conclusion, a balance was designed and fabricated at the Langley Research Center in 1980 (before the current study) that used inner and outer concentric tubes. The inner tube provides a passage for the simulant scramjet exhaust, which is injected into the model and exhausted through the scramjet nozzle. (See fig. 1.) The balance is directly exposed to the elevated temperatures of the simulant gas and indirectly affected by aerodynamic heating of the model; therefore, temperature sensitivity problems of flow-through balances are a major concern. During calibration, the balance is heated uniformly to typical operating temperatures, so that temperature gradients within the balance are not included in the calibration process. Typically, balances are watercooled to suppress temperature gradients. However, geometric constraints preclude the use of watercooling for flow-through balances in small-scale hypersonic wind tunnels. Because flow-through balances are directly exposed to the simulant gas, convective heat

transfer from this gas will develop temperature gradients within the balance that may significantly affect balance accuracy.

During the tests, a mixture by volume of 50 percent Argon and 50 percent Du Pont Freon 12 (Ar-Fr) was used to simulate scramjet exhaust. At the moderate temperatures possible in hypersonic wind tunnels, this substitute gas yields nozzle pressure distributions that closely approximate those of hydrogen and air combustion products (ref. 3). However, because Freon 12 is hazardous to the environment, the use of this product as a scramjet exhaust simulant gas has since been discontinued. Because the simulant gas replaces the scramjet exhaust, the inlet airflow must bypass the combustor nozzle. Otherwise, the mixture of inlet airflow and simulant gas would have unknown composition and expansion characteristics. To accommodate this problem, a fairing was attached to divert the airflow around the inlet. This method was more acceptable than an operable inlet because the model geometry could not accommodate the ingestion of inlet airflow and the simultaneous ejection of scramjet exhaust simulant. In addition to the effects of the simulant gas on internal heating, external aerodynamic heating can also adversely affect the accuracy of a nonwatercooled balance. Hence, the accuracy of the balance without exhaust gas simulation was also investigated.

This research was performed under the cooperative hypersonic program between the Langley Research Center and the North Carolina State University. A master's thesis resulted from this effort and is noted as reference 4. The test was conducted in the NASA Langley 20-Inch Mach 6 Wind Tunnel. This paper presents the details and results of the experimental investigation to evaluate the thermal effects on a flow-through balance with scramjet exhaust flow simulation.

Nomenclature

A	axial-force strain gauge (fig. 8(a))
Ar	Argon
F_A	axial-force balance measurement, lb
F_N	normal-force balance measurement, lb
F_Y	side-force balance measurement, lb
Fr	Freon 12
M	Mach number
M_X	rolling-moment balance measurement, in-lb

M_Y	pitching-moment balance measurement, in-lb
M_Z	yawing-moment balance measurement, in-lb
N1	forward normal-force strain gauge (fig. 8(a))
N2	aft normal-force strain gauge (fig. 8(a))
p	pressure, psia
q	dynamic pressure, psia
R_∞	free-stream Reynolds number, 1/ft
RM	rolling-moment strain gauge (fig. 8(a))
S1	forward side-force strain gauge (fig. 8(a))
S2	aft side-force strain gauge (fig. 8(a))
T	temperature, °F or °R
T	thermocouple
α	angle of attack, deg
Subscripts:	
o	tunnel stagnation conditions
st	total conditions in simulant gas storage vessel
tj	total (stagnation) jet plenum conditions
∞	free-stream conditions
1, 2, ..., 8	balance locations for thermocouples and strain gauges (fig. 8(a))

Experimental Apparatus and Methods

Test facility

This investigation was conducted in the 20-Inch Mach 6 Wind Tunnel, which is the hypersonic blow-down facility shown in figure 2. This facility employs an adjustable second minimum and exhausts either to vacuum spheres or to the atmosphere with the aid of an annular air ejector. Air is transferred from a 4250-psia tank field to a 600-psia reservoir supply with a storage capacity of 42 000 ft³ and is heated to 1000°R by an electrical resistance heater. An activated alumina dryer provides a dewpoint temperature of 419°R at a pressure of 600 psia. The operating conditions for the tunnel are stagnation pressures of 30 to 525 psia, stagnation temperatures

of 810° to 1018°R, and free-stream Reynolds numbers of 0.5 to 9.0×10^6 /ft. The wind tunnel has a two-dimensional, fixed-geometry, contoured nozzle that is 7.45 ft long. The test section is 20.5 by 20 in. and is fitted with two quartz windows for schlieren observation that are 17 in. in diameter. Typical run times are 5–10 min when the air exhausts to vacuum spheres, depending on free-stream Reynolds number, and 20 min when the air ejects to the atmosphere. A detailed description of this tunnel is presented in reference 5.

The 20-Inch Mach 6 Wind Tunnel has upper and lower injection systems within the test section. The upper injection system was used to inject a flow field pressure probe while the model was mounted on the lower injection system. This lower injection system includes a manually operated, remotely controlled model support system. Injection time of the model is approximately 1 sec with a maximum acceleration of $2g$ for force tests.

The 20-Inch Mach 6 Wind Tunnel was selected for this research effort because it has an existing propulsion simulation gas supply system. That system, which consisted of a heated 22-ft³ pressurized storage vessel, pumps, gas bottle manifolds, and control valves, supplied the simulant gas to a connection at the rear of the sting support strut. The storage vessel was evacuated with a vacuum pump before it was filled. For the simulant gas tests, the storage tank contained approximately 220 lb of 50 percent each by volume of Argon and Freon 12. This mixture was heated to 500°F with a final tank pressure of 1390 psia. Model plenum pressure was remotely controlled from a regulator valve during each run. Typical powered test run times were 1–3 min when the model plenum stagnation pressure was approximately 20 psia. Further details of the propulsion simulation system are presented in reference 6.

Model

The stainless steel HAPCM-50 model was 26 in. long by 6 in. high by 6 in. wide. Two configurations of the HAPCM-50 model were evaluated during this investigation. One was an unpowered configuration (that excluded the wing, stabilizers, fairing, and scramjet engine as shown in fig. 3), the other was a powered configuration (that excluded the wing and stabilizers but included the engine and fairing as shown in fig. 1). The model was tested without its lift and control surfaces so that the balance thermal sensitivity could be isolated from force and moment increments created by those surfaces. An installation photograph of the HAPCM-50 powered configuration

in the 20-Inch Mach 6 Wind Tunnel is shown in figure 4.

Instrumentation

Langley balance 2042 was the six-component, nonwatercooled, flow-through strain gauge balance used in this study. Figure 5 shows the assembly drawing for balance 2042, including the metric and nonmetric portions. The balance was constructed with inner and outer concentric tubes, as shown in figure 6. The outer tube was machined near each end to form strain gauge beams necessary for force measurement. The outer tube included two annular beams (see figs. 6 and 7) that measured axial force and eight rectangular beams that measured the remaining balance components. The inner and outer balance tubes were attached at the ends of the outer tube beyond the strain gauge beams. The model was attached to the "free-floating" metric section of the outer balance tube (fig. 6), which translated relative to the inner tube when an axial load was applied. The axial force was measured by eight strain gauges that were mounted on the surface of the two annular beams outside the balance lands. These beams restrained the movement of the free-floating section of the outer balance tube when an axial load was imparted on the model. The inner tube provides a passage for the simulant gas that flows through the hollow sting, into the balance, and out four circular ports near the midpoint of the balance and perpendicular to the incoming flow. (See fig. 1 for simulant gas flow path.) Then, the gas is collected in the plenum of the model and directed through the scramjet nozzle. To reduce the thermal effects of the simulant exhaust gas upon the balance, a sleeve made of Bakelite, a product of Union Carbide Corporation, was inserted into the inner balance tube.

In addition, when Langley balance 2042 was fabricated, it possessed two stainless steel bellows as non-loadbearing members to keep the simulant exhaust gas inside the inner tube from escaping around the four flow ports, thereby reducing the thermal and pressure impact on the strain gauges. Four O-rings, together with the bellows, isolate any pressure difference between the metric and nonmetric parts of the balance, both fore and aft, and allow the beams to carry the full loads for five of the six force and moment components. The bellows are flexible enough in normal, axial, and side forces as well as pitching and yawing moments, to keep the associated mechanical effects below the balance sensitivity. However, the bellows do absorb approximately 32 percent of the rolling moment. The temperature effects attributable to the bellows were negligible, but the

bellows do provide a significant amount of mass for heat transfer to occur, either from the simulant gas or from aerodynamic heating.

Wheatstone bridge strain gauge circuits were used in Langley balance 2042 to measure the normal-force, side-force, yawing-moment, pitching-moment, and rolling-moment components of the vehicle. Strain gauge locations and circuit diagrams are shown in figures 8(a) and (b), respectively. To improve balance measurement accuracy and to negate the interactions of other forces and moments, four active strain gauges were mounted on the top and bottom of two rectangular beams for each bridge circuit that measured these components. The voltage output of a wheatstone bridge is based upon a comparative measure of resistances within the circuit (ref. 7); thus, uniform temperature increases of the strain gauges within a bridge or uniform thermal expansion of the beams that support these gauges will not affect bridge output. Therefore, only temperature variations within a particular bridge structure will affect the measurement of this component. To obtain the normal-force and pitching-moment components, the measurements of bridges N1 and N2 (fig. 8(a)) were added and subtracted, respectively. Similarly, the side-force and yawing-moment components were obtained by adding and subtracting the measurements of bridges S1 and S2, respectively. Because of the complexity of measuring axial force, a double wheatstone bridge circuit with eight active strain gauges was used. As shown in figure 7, these strain gauges were mounted on the surface of the annular beams. In addition, eight thermocouples were mounted within the balance to measure the temperature variations within the balance. As shown in figure 8(a), thermocouples T₅ and T₇ were adjacent to the axial-component strain gauge bridge and thermocouples T₁ and T₂ were adjacent to the normal-force, side-force, and rolling-moment strain gauge bridges. Thermocouples T₃, T₄, T₆, and T₈ were mounted on the annular beam. These thermocouples should also reveal the heat transfer from the model to the balance.

The thermal sensitivity of Langley balance 2042 was determined by calibration in a thermally controlled oven in which the balance was heated uniformly to 180°F. Then, the drift in the voltage output of each bridge circuit was adjusted by the addition of segments of temperature-sensitive wire to the appropriate circuits; this drift had been caused by slight variations in the resistivities of the strain gauges within a particular circuit. Thereafter, the balance primary sensitivity was verified at 180°F during temperature calibration. The sensitivity of the

balance was 0.5 percent of full-scale (maximum) load, which is typical for most balances. As indicated by the sensitivity, the balance was unable to accurately measure forces and moments less than 0.5 percent of full scale. The full-scale loads for the six balance components are listed in table I. Thus, the balance sensitivity was unaffected by uniform temperature increases.

Table I. Load Limits on Langley Balance 2042

Force:	
F_N , lb	100
F_A , lb	20
F_Y , lb	50
Moment:	
M_Y , in-lb	200
M_X , in-lb	100
M_Z , in-lb	100

Results and Discussion

Experimental Test Procedure

The balance heating effects were evaluated through the tunnel stagnation pressure range of 30 to 475 psia and the stagnation temperature range of 410° to 475°R. These conditions correspond to free-stream Reynolds numbers in the 20-Inch Mach 6 Wind Tunnel of 0.5 to $7.4 \times 10^6/\text{ft}$. For the powered configuration, three simulant exhaust gases were tested in the model: cold air, hot air, and Ar-Fr. For the cold- and hot-air simulant gas tests, the simulant gas storage vessel contained approximately 100 lb of air at 1500 psia. The stagnation temperatures of the cold and hot air were 200° and 500°F, respectively. The simulant gas flow rate was remotely controlled to maintain a plenum stagnation pressure of 20 psia. The test matrix in table II provides a detailed description of the test conditions.

During each run, the model was mounted on a sting-support strut and was injected into the airstream after the tunnel flow was established. This normal operating procedure prevents possible damage to the force balance from large transient loads when a starting shock wave passes through the test section of the tunnel with the model positioned there. For the powered simulation tests, the simulant gas flow began after the model was positioned within the test section. The stagnation temperature and pressure of the simulant exhaust gas were measured within the plenum of the simulated scramjet engine. For each test, time histories of the balance temperatures and the six force and moment components were

monitored and recorded. In addition, the base pressures and chamber pressure of the model were measured by 20- and 50-psia transducers, respectively, to exclude those contributions to the overall balance forces and moments.

Table III provides the data from this test in tabular format. Each run outlined in table II is presented with time as the dependent variable and contains the corrected force and moment balance measurements (including sting-balance deflections and base-chamber pressure corrections) as well as the time histories of the balance thermocouple measurements. Because the concern was evaluation of the flow-through balance and not vehicle performance, the force and moment data are presented in engineering units.

Balance Thermal Effects Without Simulant Gas Flow

Acquisition of complete configuration aerodynamic forces and moments with the scramjet engines properly simulated requires that the flow-through balance be used to measure the forces and moments with and without simulant gas flow. The aerodynamic heating at the surface of the model may affect the balance measurements when the balance is not watercooled. Hence, the balance thermal effects attributable to aerodynamic heating were evaluated for two configurations of the HAPCM-50, the unpowered configuration and the powered configuration without simulant gas flow. Zero shifts in balance components from thermal and other effects are defined as the difference between the wind-off balance measurements before model injection and after model retraction with the tunnel at atmospheric pressure. In general, the zero shifts should indicate the accuracy of the six balance measurements during a particular test. To correlate zero shifts in the balance measurements with balance temperatures, time histories of various balance temperatures and three balance measurements were evaluated for various Reynolds numbers and angles of attack.

To understand the thermal effects of external aerodynamic heating upon the balance measurements, a qualitative analysis of heat transfer within the model and balance is necessary. Basically, the aerodynamic heating on the model was conducted through the surface and entered the balance primarily through the balance lands. (See fig. 7.) Once inside, the heat was trapped by the axial web structure (see fig. 6), which included an annular beam and four 1/16-in. rectangular beams that connect the ends of the outer tube to the center of the balance. The narrow passages of these beams effectively trap

the heat that enters through the lands. As a result, the temperatures within the center of the outer tube increased for the high-pressure runs ($R_\infty = 7.43 \times 10^6/\text{ft}$), as illustrated by the time histories of thermocouples T_5 and T_8 in figure 9. Because of the web structure, the heat transfer rate was significantly reduced within the forward and aft ends of the balance and the temperature increased only moderately at the ends. In general, the temperature increase within the ends of the outer balance tube was 70 percent less than the temperature increase near the balance lands, as demonstrated by thermocouples T_1 and T_2 in figure 9. Therefore, the strain gauge bridges that were closest to the balance lands should be most affected by aerodynamic heating at the surface of the model for the axial-force measurement F_A .

For the unpowered tests, the normal force F_N , side force F_Y , pitching moment M_Y , rolling moment M_X , and yawing moment M_Z were unaffected by aerodynamic heating, as shown in figure 10 (longitudinal data only). The maximum zero shift for any of these measurements was 0.5 percent. Table IV illustrates this situation for F_N and M_Y . Because the balance sensitivity was 0.5 percent of full scale, the zero shifts were negligible. Conceivably, these balance measurements were unaffected by the aerodynamic heating at the model surface because of the location and structure of their respective strain gauge bridges—these bridges were at the ends of the outer balance tube; hence, they were more isolated from the effects of aerodynamic heating than the others. The temperature increase for the highest aerodynamic heating ($R_\infty = 7.47 \times 10^6/\text{ft}$) near these bridges (thermocouples T_1 and T_2) was much smaller than temperature increases near the lands. The maximum temperature increase in thermocouples T_1 and T_2 was 11° and 1°F , respectively. However, near the balance lands, the maximum temperature rise was 35°F . The strain gauges in each bridge circuit were mounted circumferentially at a given cross-sectional plane of the balance; thus, only circumferential temperature gradients will affect these balance measurements. Unfortunately, only one thermocouple was placed at the forward and aft locations of these bridges (fig. 8(a)), so the circumferential temperature gradients could not be measured. Although the measurements of F_N and M_Y required outputs from two bridges at opposite ends of the balance (bridges N1 and N2 in fig. 8(a)), these bridge measurements were independent of each other. Therefore, axial temperature gradients within the balance will not affect these measurements, nor will they affect the measurements of F_Y and M_Z . In short, F_N , F_Y , M_Y , M_X , and M_Z were unaffected by

aerodynamic heating at the model surface because their respective bridge circuits are isolated from the aerodynamic heating.

Ideally, the flow-through balance F_A should be unaffected by axial temperature variations as well. The free-floating design of the outer balance tube and the structure of the axial-component bridge circuit should minimize the sensitivity of F_A to axial temperature variations. Recall that the double bridge circuit that measures axial force included eight strain gauges mounted on two annular beams. (See figs. 7 and 8.) The two sections of this circuit are mounted on the forward and aft annular beams. This circuit electrically averages the resistances of the strain gauges under tensile strains and averages the gauges under compressive strains. For example, when a positive axial load is applied to the balance, strain gauges A_1 , A_3 , A_5 , and A_7 (fig. 8(a)) undergo tensile strains as the remaining gauges are compressed. This double bridge circuit uses a comparative measure of the resistances within the circuit to obtain the voltage output (like the wheatstone bridge circuits of the other balance components). Hence, provided the temperature in each annular beam increases uniformly, the voltage output of the double bridge circuit will be unaffected by thermal expansion of the annular beams.

Unlike the other balance components, the axial-force measurements were affected by aerodynamic heating at the model surface, as shown in table IV. The magnitude of the zero shifts in the axial component for the unpowered configuration varied from 0.7 to 4.7 percent for the low-pressure runs ($R_\infty \leq 4 \times 10^6/\text{ft}$). For the high-pressure runs ($R_\infty \approx 7 \times 10^6/\text{ft}$), these shifts ranged from 3.1 to 10.4 percent. Typically, zero shifts are representative of the variation in balance measurements during a test. In a few instances, however, the zero shifts in F_A for the flow-through balance were not representative during the run, caused in part by the time that had elapsed between when the model was retracted from the test section and when the tunnel returned to atmospheric pressure. This additional time allowed the heat to redistribute within the model and balance, thus affecting the axial-component zero shift, which was measured after the tunnel reached atmospheric conditions.

Determination of the balance thermal effects of F_A during the tests required that the shift in axial force be tabulated between the time of model injection and retraction for each test, as shown in table V. However, the measurement immediately after model injection was excluded because vibrations of the model, sting, and balance may affect the balance measurements. Instead, the measurement 5 sec after

injection was used to define the axial-force shift during the run. During the low-pressure runs, the magnitude of the shift ranged from 0.3 to 1.4 percent; for the high-pressure runs, this shift varied from 1.8 to 4.2 percent. As expected, as the free-stream Reynolds number increased from 0.5 to $7 \times 10^6/\text{ft}$ (p_o increased from 30 to 475 psia), the aerodynamic heating at the model surface increased, but the aerodynamic heating for $R_\infty < 1 \times 10^6/\text{ft}$ had a negligible effect on F_A . The balance temperatures did not increase more than 2°F , and the axial-force shifts were less than balance sensitivity. As illustrated in figures 11 and 12, the balance temperatures were essentially constant in both unpowered and powered configurations for $R_\infty \approx 0.5 \times 10^6/\text{ft}$. However, for $R_\infty \approx 7 \times 10^6/\text{ft}$, the aerodynamic heating significantly affected F_A . As shown in figures 13-15, the balance temperatures adjacent to the balance lands (thermocouples T_5 and T_8) increased by 20° to 30°F . Furthermore, the corresponding axial-force measurements for the unpowered configuration at $\alpha = 0^\circ$ and 5° shifted by 4.2 and 2.8 percent, respectively, while in the flow, as shown in figures 14 and 15.

In all the runs without gas simulation, F_A decreased throughout the tests. For this flow-through balance, a 1-percent shift in the force and moment measurements was considered acceptable. Therefore, the axial-force measurements of the flow-through balance for $R_\infty \leq 1 \times 10^6/\text{ft}$ were acceptable throughout these tests (approximately 80 sec). However, this measurement on the HAPCM-50 was not acceptable for the runs in which $R_\infty > 1 \times 10^6/\text{ft}$, which lasted to 110 sec. So, unlike the other five balance components, the axial-force measurements of the flow-through balance were adversely affected by aerodynamic heating at the model surface.

Because the outer balance tube was a free-floating design, nonuniform thermal expansion caused by axial temperature variations would not have affected F_A if the balance were ideally constructed. For example, aerodynamic heating causes the center of the outer balance tube to expand while the inner balance tube and the ends of the outer balance tube remain thermally isolated because of the web structure designed into the outer balance tube. The free-floating section of the outer balance tube remains in static equilibrium, so the axial force on the two annular beams from thermal expansion will be equal in magnitude and opposite in direction. If the balance engineers designed the two annular beams with the same geometry, material properties, and strain gauge locations, the resistance measurements of the forward

and aft sections of the double bridge circuit would be unaffected by axial thermal expansion. However, the geometry of the annular beams is only as accurate as the tolerances of the balance design. For this case, the thickness (and tolerance) of the annular beams was 0.0253 ± 0.0005 in. The strain at the surface of an annular beam is known to be inversely proportional to the moment of inertia about the bending axis. For the most extreme case, the thicknesses of the two annular beams correspond to the upper and lower values including tolerance, namely, 0.0248 and 0.0258 in. For these two thicknesses, the moments of inertia for the beams about the bending axis would differ by 11 percent; therefore, the strains at the surfaces of the two annular beams could differ by the same amount. As a result, the axial loads caused by nonuniform axial thermal expansion of the balance may not cancel within the double bridge circuit.

Two possible improvements could have been incorporated to eliminate the sensitivity of the flow-through balance to axial temperature gradients. One improvement could have been stricter tolerances for the machined annular beams. The better and more effective alternative would be an additional step in the calibration of the flow-through balance, during which the voltage outputs of the forward and aft sections of the double bridge circuit would be measured separately when an axial load is applied. Essentially, this measurement would indicate whether the strains at the surface of both annular beams were of equal magnitude. Resistive wire could then be added so that the circuits would have the same sensitivity. As a result, the axial forces on the two annular beams from axial thermal expansion would not affect the axial-force measurement of the flow-through balance.

The combined effects of axial bridge location and structure that resulted in thermal sensitivity of the axial component have been discussed. The strain gauge bridge circuits of this component were mounted in the annular beams that were the closest force-measuring structures to the balance lands. (See fig. 8(a).) This region had the highest heat transfer rates because the balance lands were the primary path of heat conduction into the balance. Both thermal expansion of the outer tube and circumferential temperature variations within the annular beams probably caused axial-force shifts. For the high-pressure runs, the temperature in the free-floating section of the outer balance was 15° – 20° F higher than the rest of the balance near the end of the runs. The thermal expansion of this section produced equal and opposite axial forces on the

two annular beams that measured axial force. The strains within the two sections of the axial bridge circuit might not have canceled, which would affect F_A . As each run progressed, the thermal expansion of the free-floating section increased with temperature (thermocouples T_5 and T_8) which resulted in an axial-force shift that may have increased because of this expansion. (See figs. 14 and 15.) At the end of the high-pressure runs, an 8° F temperature variation was measured within this annular beam; as a result, the thermal expansion was not uniform. Because the bridge circuit can compensate only for uniform changes in the resistances of strain gauges within each of the two sections of the axial double bridge circuit, the temperature variations within the forward annular beam contributed to the shift in F_A . Also, because the annular beams were not heated uniformly, the circumferential temperature varied in the free-floating section of the outer balance tube. These temperature variations could cause nonuniformities in the thermal expansions of the 1/16-in. rectangular beams. This variation would also contribute to axial-force shifts by deflecting the annular beams nonuniformly. In conclusion, the axial-force measurements of the flow-through balance were significantly affected by circumferential temperature variations near the annular beams and possibly by thermal expansion of the free-floating section of the outer balance tube.

In typical hypersonic force and moment tests without simulant exhaust gas, the balances are watercooled; hence, balance thermal effects do not restrict the run times. Because packaging limitations affected the flow-through balances, Langley balance 2042 was not watercooled; thus, balance thermal effects restricted the allowable length of runs with a flow-through balance. For the hypersonic test method used for the HAPCM-50, the balance measurements were considered accurate to a shift of 1 percent of full scale. The axial-force shifts increased as each run progressed, so the time span could be obtained for accurate measurements. Based on a 1-percent shift, the axial-force measurements on the HAPCM-50 were accurate throughout the entire run when $R_{\infty} \leq 1 \times 10^6$ /ft. For 1×10^6 /ft $< R_{\infty} \leq 4 \times 10^6$ /ft, the axial-force balance measurements were accurate within 30 sec of model injection, the balance temperatures for these tests having begun to increase 20–25 sec after injection. The more pronounced aerodynamic heating at $R_{\infty} \approx 7 \times 10^6$ /ft caused the balance temperatures to rise only 10 sec after model injection. As a result, these measurements were accurate only to about 20 sec after injection.

Balance Thermal Effects With Simulant Gas Flow

The main objective of this investigation was to evaluate the accuracy of the flow-through balance during simulant exhaust gas runs. Three simulant exhaust gases—cold air, hot air, and 50 percent each of an Ar-Fr mixture—were tested in the powered configuration of the HAPCM-50. The cold- and hot-air gases were necessary to consider the balance thermal effects of simulant gases at different temperatures because the temperature of the Ar-Fr mixture could not be reduced without the possibility of liquefaction during nozzle expansion. Balance thermal effects were evaluated with cold-air, hot-air, and Ar-Fr simulant exhaust gases for $R_\infty \approx 0.5$ and $7 \times 10^6/\text{ft}$ at $\alpha = 0^\circ$ and 5° , as shown in the test matrix (table II).

Thermal effects of simulant gas flow on balance. The simulant gas runs at $R_\infty \approx 0.5 \times 10^6/\text{ft}$ were used to isolate the heat transfer from the simulant gas to the balance (recall that the effect of aerodynamic heating was negligible at this Reynolds number). The cold air, hot air, and Ar-Fr mixture were heated to 200° , 500° , and 500°F , respectively, in the simulant gas storage tank; however, thermal losses in the simulant gas supply lines to the model held the jet total temperatures (T_{tj}) within the balance to only 96° , 196° , and 227°F , respectively. The value T_{tj} actually increased during each run (figs. 16–18) as a result of the increasing temperatures in the simulant gas supply system from the storage tank to the model. Although the Bakelite sleeve insulated the inner balance tube, the inner tube was noticeably heated by the simulant gases, especially by the hot air and Ar-Fr, as shown in figures 17 and 18. The heat within this tube conducted into the outer balance tube primarily through the common attachment point at the aft end of the balance, as exemplified by the increase in thermocouple T_2 in figures 16–18. Unlike the aft end of this balance, the forward section was isolated from the thermal effects of the simulant gas because the gas exited the balance through the four cylindrical nozzles between the balance lands. (See fig. 7.) Thus, the forward section of the balance was not exposed to the high temperatures of these gases. In general, the temperature rise within this region was one-third the temperature rise within the aft end of the balance. (Compare thermocouples T_2 and T_1 in figs. 16 and 17.)

The F_N , F_Y , M_Y , M_X , and M_Z measurements were unaffected by the balance thermal effects of the simulant exhaust gases, as shown in figure 19 for the longitudinal data. In general, the zero shifts of these measurements (which were indicative of the

component shifts during the runs) did not exceed the balance sensitivity. (See table IV.) The heat transfer from the simulant gases had a negligible effect on these balance measurements for two likely reasons: first, the strain gauge bridge structures at the front of the balance (bridges N1 and S1 in fig. 8(a)) were isolated from the simulant gas thermal effects; second, the convective heat transfer from the simulant gases was symmetrical about the centerline of the inner balance tube near the aft strain gauge bridge structures. (See bridges N2, S2, and RM in fig. 8(a).) The isolation of the forward strain gauge bridges from thermal effects can be confirmed by a review of figures 16–18, which showed that temperature rises at the front of the balance are relatively small. As for the axisymmetric nature of the simulant gas flow, the strain gauge beams that measured bridges N2, S2, and RM were adjacent to the inner and outer balance tube attachment points. (See fig. 8(a).) Hence, the temperature of these beams and their corresponding bridge circuits increased dramatically in comparison with the rest of the outer balance tube. As illustrated in figure 18, the temperature of thermocouple T_2 increased by as much as 65°F for the simulant gas runs. Although the temperatures of these bridges increased dramatically, the balance measurements of F_N , F_Y , M_Y , M_X , and M_Z were unaffected because the temperatures of these bridges increased uniformly. Aforementioned, uniform increases in temperatures within a bridge will not affect the bridge output. The uniformity in balance temperatures at cross sections in the aft section of the outer balance tube is illustrated by the temperatures within the aft annular beam. (See thermocouples T_6 and T_7 in figs. 16–18.) The maximum temperature difference within this beam for all simulant gas runs was 3.4°F . Therefore, if axisymmetrical pipe flow was established within the inner balance tube (a circular cylinder), the convective heat transfer and temperature from the simulant gases will be symmetrical about the centerline.

Unlike the other balance components, the axial-force measurements were significantly affected by the balance heating of the three simulant exhaust gases. For the low-pressure tunnel conditions, the average axial-force zero shift for the runs with cold air, hot air, and Ar-Fr was 1.7, 3.3, and 5.1 percent, respectively. The hot-air and Ar-Fr simulant exhaust gas runs showed a larger increase in the axial-force zero shifts compared with the shifts for the cold-air simulant exhaust gas, primarily from the increase in total temperature of these gases. The runs with hot air and Ar-Fr were 100° and 150°F higher, respectively, than the cold-air total temperature.

Because the temperature increases within the forward and aft annular beams were essentially uniform for the low Reynolds number ($R_\infty \approx 0.5 \times 10^6/\text{ft}$) simulant gas run (see figs. 16-18 in which forward temperatures (thermocouples T_3 and T_4) and aft temperatures (thermocouples T_6 and T_7) are compared), the balance measurements were primarily affected by thermal expansion of the inner and outer balance tubes. The inner balance was directly exposed to the heat transfer from the simulant gas; thus, this tube should thermally expand more than the outer balance tube. Also, the annular beams in the outer balance tube exhibited additional axial forces from thermal expansion of the inner tube. Conceivably, because the strains within the annular beams after thermal expansion of the inner tube did not cancel within the double bridge circuit, they did cause an axial-force shift.

In general, the balance heating from the hot-air and Ar-Fr simulant exhaust gases was more pronounced than the aerodynamic heating from the external tunnel flow. For the hot-air and Ar-Fr simulant gases, the balance temperatures began increasing 5 sec after model injection, whereas the balance temperatures began increasing 10 sec after model injection for the high tunnel-pressure tests without simulant gas flow. The more pronounced balance heating from the simulant gases was expected because the balance was directly exposed to the high temperatures of the hot air and Ar-Fr, whereas the aerodynamic heating at the model surface must conduct through the stainless steel model before that heat affects the balance.

Combined thermal effects of simulant gas flow and aerodynamic heating on balance. As before, the F_X , F_Y , M_Y , M_X , and M_Z measurements were unaffected by the combined thermal effects of tunnel flow and simulant gas flow. However, the axial-force measurements were significantly affected by the combined thermal effects of tunnel flow and exhaust gas simulation. The average axial-force zero shifts for the high tunnel-pressure runs ($R_\infty \approx 7 \times 10^6/\text{ft}$) with cold-air, hot-air, and Ar-Fr exhaust simulation were 2.6, 6.0, and 7.7 percent, respectively. As expected, the balance thermal effects from aerodynamic heating at the model surface for the high tunnel-pressure simulant gas runs caused an increase in the axial-force zero shifts relative to the low tunnel-pressure simulant gas runs. As illustrated by thermocouples T_6 and T_7 in figures 20-22, the temperature varied within the annular beams, which was not the case for the low tunnel-pressure simulant exhaust gas runs. The temperature variations within the annular beams were a direct result

of aerodynamic heating at the model surface. At the end of the high tunnel-pressure runs with exhaust simulation, the temperature variations within the aft annular beam were 5°, 9°, and 11°F for the cold-air, hot-air, and Ar-Fr runs, respectively. These temperature gradients were the primary cause for the increased zero shifts of the high tunnel-pressure runs relative to the low tunnel-pressure simulant exhaust gas runs.

The axial force decreased throughout the cold- and hot-air exhaust simulation runs as illustrated in figures 20 and 21, respectively. As the value T_{ij} increased, the balance thermal effects were more pronounced. Unlike the cold- and hot-air exhaust simulation runs, the axial force did not stabilize for the Ar-Fr exhaust simulation runs (see fig. 22) because the exhaust gas controls could not maintain the desired plenum stagnation pressure of 20 psia. Thus, the thrust oscillations from the simulant exhaust gas caused F_A to oscillate. As shown in figures 20-22, the plenum total pressure p_{ij} oscillations were in phase with the axial-force oscillations. Because the plenum pressure must stabilize before the forces and moments can be measured, the run time for simulant exhaust gas tests is highly dependent upon the ability of the exhaust gas automatic controller to reach the desired plenum stagnation pressure. For the simulant exhaust gas runs of this investigation, this controller was not adequate and the settling time of the plenum stagnation pressure ranged from 20 to 80 sec. The axial-force shifts increase as the test run progresses, so a controller with sufficient damping is highly desirable to minimize the run time when the balance thermal effects are a major concern. The overshoot and settling time for the plenum stagnation pressure can be minimized if the controller can be properly damped.

Therefore, as for the runs without exhaust gas simulation, accurate axial-force measurements can be obtained at the beginning of these tests. Unfortunately, a time span for accurate (less than 1 percent of full scale) F_A could not be defined because of the oscillations at the beginning of these runs. However, the balance temperatures began increasing 10 sec after injection of the HAPCM-50 for the cold-air simulant exhaust gas runs. This change suggests that accurate measurements can be obtained for at least 10 sec after model injection. Similarly, accurate measurements can be obtained 5 sec after model injection for the hot-air and Ar-Fr simulant exhaust gas runs.

Concluding Remarks

A flow-through balance was used to evaluate the thermal effects of scramjet exhaust flow simulation

and aerodynamic heating on the force and moment measurements for the hypersonic, airbreathing-propulsion cruise missile (HAPCM-50) model. The normal-force, side-force, yawing-moment, rolling-moment, and pitching-moment balance measurements were unaffected by the balance heating produced by exhaust gas simulation and wind tunnel flow. In general, the zero shifts of these components were less than balance sensitivity (0.5 percent of full scale). However, the balance axial-force measurements were significantly affected by balance heating on the HAPCM-50. For the runs with the highest aerodynamic heating (free-stream Reynolds number of about $7 \times 10^6/\text{ft}$) without exhaust gas simulation, the axial-force shifts ranged from 1.8 to 4.2 percent. For these runs, the axial-force measurements were accurate (less than a 1-percent shift) to 20 sec after the model was injected into the test section. For the exhaust simulations with cold air, hot air, and 50 percent each by volume of Argon and Freon (Ar-Fr), the average zero shifts were 2.1, 4.6, and 6.4 percent, respectively. The axial-force shifts could have been reduced if the forward and aft sections of the axial-force bridge circuit had been independently calculated. During the runs with simulant exhaust gas, the axial-force measurements were accurate to 10 sec after model injection for cold-air exhaust simulation and only to 5 sec for the hot-air and Ar-Fr exhaust simulation runs. Because the plenum pressure must stabilize before the forces and moments can be measured, the run time for simulant gas runs is highly dependent upon the ability of the simulant gas automatic controller to reach and maintain the desired plenum stagnation pressure. Therefore, a controller with sufficient damping is highly desirable to minimize the run time when thermal effects are a concern.

Within the scope of the investigation, nonwater-cooled, flow-through balances with this design are not practical for scramjet exhaust flow simulation tests. Nonwatercooled balances will not provide accurate axial-force measurements except at the beginning of the test and the time span for accurate

measurements is highly restrictive. Even if an adequate plenum pressure controller is available for the simulant gas system of the facility, during hot-air and Ar-Fr exhaust simulations, the time span is sufficient only to evaluate one condition (i.e., angle of attack, plenum pressure, etc.). In typical force and moment tests, an entire angle-of-attack sweep is evaluated for each test if sufficient run time is available. Also, adequate time is required between runs for the model to cool. (Cooling took as much as 1 hr for the current model.) In general, a heated exhaust gas may produce unacceptable force and moment uncertainties when used with thermally sensitive balances.

NASA Langley Research Center
Hampton, VA 23681-0001
February 26, 1993

References

1. McClinton, Charles R.; Bittner, Robert D.; and Kamath, Pradeep S.: CFD Support of NASP Design. AIAA-90-5249, Oct. 1990.
2. Hartill, William R.: *Method for Obtaining Aerodynamic Data on Hypersonic Configurations With Scramjet Exhaust Flow Simulation*. NASA CR-2831, 1977.
3. Oman, R. A.; Foreman, K. M.; Leng, J.; and Hopkins, H. B.: *Simulation of Hypersonic Scramjet Exhaust*. NASA CR-2494, 1975.
4. Kniskern, Marc W.: Analysis of a Six-Component, Flow-Through, Strain-Gage, Force Balance Used for Hypersonic Wind Tunnel Models With Scramjet Exhaust Flow Simulation. M.S. Thesis, North Carolina State Univ., 1990.
5. Keyes, J. W.: *Force Testing Manual for the Langley 20-Inch Mach 6 Tunnel*. NASA TM-74026, 1977.
6. Cabbage, James M.; and Monta, William J.: *Parametric Experimental Investigation of a Scramjet Nozzle at Mach 6 With Freon and Argon or Air Used for Exhaust Simulation*. NASA TP-3048, 1991.
7. Holman, J. P.: *Experimental Methods for Engineers*, Fifth ed. McGraw-Hill, c.1989.

Table II. HAPCM-50 Configuration and Nominal Condition Test Matrix

R_∞, ft^{-1}	p_o, psia	$T_o, ^\circ\text{F}$	α, deg
Unpowered configuration			
0.5×10^6	30	410	-3.5
$.5 \times 10^6$	30	↓	0
$.5 \times 10^6$	30	↓	5.0
1.0×10^6	60	↓	0
2.0×10^6	125	450	-3.5
2.0×10^6	125	↓	0
2.0×10^6	125	↓	5.0
4.0×10^6	250	↓	0
7.0×10^6	475	475	-3.5
7.0×10^6	475	475	0
7.0×10^6	475	475	5.0
Powered configuration; jet off			
0.5×10^6	30	410	0
$.5 \times 10^6$	30	410	5.0
7.0×10^6	475	475	0
7.0×10^6	475	475	5.0
Powered configuration; cold air: $p_{tj} = 20 \text{ psia}$; $T_{st} = 200^\circ\text{F}$			
0.5×10^6	30	410	0
$.5 \times 10^6$	30	410	5.0
7.0×10^6	475	475	0
7.0×10^6	475	475	5.0
Powered configuration; hot air: $p_{tj} = 20 \text{ psia}$; $T_{st} = 500^\circ\text{F}$			
0.5×10^6	30	410	0
$.5 \times 10^6$	30	410	5.0
7.0×10^6	475	475	0
7.0×10^6	475	475	5.0
Powered configuration; Ar-Fr: $p_{tj} = 20 \text{ psia}$; $T_{st} = 500^\circ\text{F}$			
0.5×10^6	30	410	0
$.5 \times 10^6$	30	410	5.0
7.0×10^6	475	475	0
7.0×10^6	475	475	5.0

Table III. Tabular HAPCM-50 Test Data From 20-Inch Mach 6 Wind Tunnel Test

Δt (sec)	F_N	F_A	M_Y	M_X	M_Z	F_Y	T_1	T_2	T_3	T_4	T_5	T_6	T_7	T_8
Unpowered configuration; $M_\infty = 5.79$; $R_\infty = 0.63 \times 10^6$ /ft; $\alpha = -3.45^\circ$; T_{ij} and p_{ij} not applicable														
0	-0.02	-0.02	0.06	0.03	-0.01	0.13	83.1	83.7	84.8	82.5	79.8	82.0	81.2	78.6
31.52	-.77	.25	-1.86	.17	.07	.02	↓	↓	84.7	82.5	79.9	↓	↓	78.7
37.58	-.79	.24	-1.87	.13	.07	.02	↓	↓	↓	82.5	79.9	↓	↓	78.6
42.19	-.78	.23	-1.89	.17	.05	.01	↓	↓	↓	82.4	79.9	↓	↓	78.7
47.44	-.79	.22	-1.91	.13	.07	.02	83.0	83.6	↓	82.4	80.0	81.9	↓	78.6
52.56	-.81	.22	-1.88	.17	.07	.02	83.1	↓	↓	82.5	80.1	82.0	↓	78.7
57.06	-.82	.21	-1.92	.17	.07	.02	83.1	↓	↓	82.5	80.3	↓	81.3	78.7
61.47	-.79	.20	-1.92	.13	.09	.01	83.1	↓	↓	82.4	80.3	↓	81.3	78.7
67.38	-.82	.19	-1.91	.13	.07	.02	83.2	↓	↓	82.4	80.6	↓	81.4	78.8
72.44	↓	.18	-1.91	.17	↓	.02	83.2	↓	↓	82.4	80.7	↓	81.5	78.8
79.81	↓	.17	-1.93	.13	↓	.02	83.3	↓	↓	82.5	81.0	↓	81.6	78.9
83.92	↓	.17	-1.92	.18	↓	0	83.4	83.5	↓	82.5	81.1	↓	81.7	79.0
88.82	↓	.16	-1.92	.17	.09	.01	83.5	83.6	↓	82.6	81.3	82.1	81.8	79.1
94.24	↓	.15	-1.92	.17	.09	.01	83.6	83.6	↓	82.6	81.6	82.1	81.9	79.1
100.25	-.83	.14	-1.90	.17	.05	.01	83.6	83.5	↓	82.6	81.8	82.2	82.0	79.3
105.06	-.83	.14	-1.90	.18	.07	0	83.7	83.5	↓	82.7	82.1	82.2	82.1	79.4
114.77	-.06	-.49	.11	.05	-.03	.11	83.9	83.6	↓	82.8	82.5	82.3	82.3	79.6
Unpowered configuration; $M_\infty = 5.80$; $R_\infty = 0.63 \times 10^6$ /ft; $\alpha = -0.04^\circ$; T_{ij} and p_{ij} not applicable														
0	0.08	-0.12	0.02	-0.01	0.13	0.20	83.1	83.9	84.0	82.7	80.7	83.5	82.8	81.3
13.03	.20	.78	.71	-.03	.19	.11	↓	↓	↓	82.7	80.8	↓	↓	81.3
22.50	.20	.75	.75	-.02	.18	.11	↓	↓	↓	82.7	80.8	↓	↓	81.1
30.11	.21	.73	.78	-.03	.20	.10	↓	↓	↓	82.8	80.9	↓	↓	81.3
35.17	↓	.72	.77	-.03	.20	.10	↓	↓	↓	↓	80.9	↓	↓	81.3
39.98	↓	.72	.77	-.02	.22	.11	83.2	↓	84.1	↓	81.0	↓	82.9	81.1
47.34	↓	.71	.78	-.02	.22	.11	83.2	↓	84.0	↓	81.0	↓	↓	↓
52.80	↓	↓	.76	-.03	.21	.10	83.1	↓	↓	82.7	81.1	↓	↓	↓
58.61	.20	↓	.80	↓	↓	↓	83.2	↓	↓	82.7	81.2	83.4	↓	↓
63.57	↓	↓	.81	↓	↓	↓	83.3	↓	↓	82.8	81.3	83.5	83.0	81.5
69.09	↓	.70	.79	↓	↓	↓	83.2	83.8	↓	82.7	81.3	83.5	83.0	81.5
77.45	↓	.69	.80	-.07	↓	↓	83.3	83.9	↓	82.8	81.6	83.6	83.1	81.6
82.86	.19	↓	.77	-.07	↓	↓	83.4	83.8	↓	82.8	81.7	83.5	83.1	81.7
88.72	.19	↓	.77	-.08	.22	.09	83.5	83.9	↓	82.9	81.9	83.6	83.2	81.8
92.88	.17	↓	.80	-.07	.22	.09	83.5	83.9	↓	82.9	82.0	83.6	83.3	81.8
106.81	.08	.02	.05	-.01	.11	.18	83.6	83.9	↓	83.0	82.3	83.7	83.4	82.1

Table III. Continued

Δtime	F_N	F_A	M_Y	M_X	M_Z	F_Y	T_1	T_2	T_3	T_4	T_5	T_6	T_7	T_8
Unpowered configuration; $M_\infty = 5.79$; $R_\infty = 0.57 \times 10^6/\text{ft}$; $\alpha = -5.00^\circ$; T_{ij} and p_{ij} not applicable														
0	0.11	0.01	0.42	0.02	0	0.14	84.6	84.8	85.7	84.1	82.0	83.9	83.2	81.3
14.63	1.60	.64	3.72	0	.07	.11	84.6	84.8	85.7	84.2	82.1	83.9	↓	81.3
20.49	1.62	.61	3.75	.01	.09	.12	84.7	84.9	85.8	↓	↓	84.0	↓	81.4
31.06	1.63	.58	3.77	0	.07	.11	84.7	84.9	85.8	↓	↓	84.0	↓	↓
35.72	↓	.58	3.78	-.04	.09	.12	84.7	84.8	85.7	↓	↓	83.9	↓	↓
40.78	↓	.57	3.78	-.04	.11	.11	84.6	↓	↓	84.1	↓	↓	↓	↓
46.04	↓	.57	3.76	0	.09	.10	↓	↓	↓	84.1	↓	↓	↓	↓
50.95	↓	.57	3.77	0	↓	↓	↓	↓	↓	84.1	82.2	↓	↓	81.5
57.36	↓	.56	3.78	-.04	↓	↓	↓	↓	↓	84.2	82.3	↓	↓	81.5
62.32	↓	↓	3.78	-.04	↓	↓	84.7	↓	↓	↓	82.3	84.0	83.3	81.6
65.83	↓	↓	3.77	-.04	↓	↓	↓	↓	↓	↓	82.4	↓	83.3	81.7
71.59	↓	↓	3.77	-.05	.11	.09	↓	↓	↓	↓	82.5	↓	83.4	81.7
76.20	1.62	.55	3.75	-.04	.11	.09	↓	84.7	85.6	↓	82.5	↓	83.4	81.7
81.31	1.60	↓	3.77	-.09	.11	.07	84.8	↓	↓	↓	82.6	↓	83.4	81.8
85.71	1.59	↓	3.74	-.05	.16	.06	↓	↓	↓	84.3	82.7	84.1	83.5	81.9
90.22	1.58	↓	3.72	-.05	.09	.06	↓	↓	↓	84.3	82.7	84.1	83.5	82.0
94.88	1.58	↓	3.71	-.09	.07	.11	↓	↓	↓	84.4	82.8	84.1	83.5	82.1
98.74	1.60	.54	3.72	-.10	.12	.06	84.9	↓	↓	84.4	82.9	84.2	83.6	82.2
106.60	.10	-.16	.39	.01	.03	.12	84.9	↓	↓	84.4	83.0	84.2	83.6	82.3
Unpowered configuration; $M_\infty = 5.85$; $R_\infty = 1.81 \times 10^6/\text{ft}$; $\alpha = -0.08^\circ$; T_{ij} and p_{ij} not applicable														
0	0.04	0	0.39	-0.08	-0.44	0.14	82.8	83.1	81.4	82.3	79.8	81.7	80.9	78.7
17.49	.14	1.60	1.41	-.08	.06	.08	↓	↓	81.4	↓	79.8	↓	↓	↓
24.80	.14	1.55	1.41	-.12	.07	↓	↓	↓	81.4	↓	79.8	↓	↓	↓
30.16	.14	1.53	1.42	-.12	.07	↓	↓	↓	81.3	↓	79.9	↓	↓	↓
34.47	.15	1.52	1.42	-.07	.07	↓	↓	↓	81.3	↓	79.9	↓	81.0	↓
39.63	↓	1.51	1.43	↓	.06	.09	82.9	↓	81.4	↓	80.0	↓	81.0	78.8
44.99	↓	1.50	1.43	↓	.07	.08	↓	↓	81.4	↓	80.1	↓	81.1	78.8
49.65	↓	1.50	1.44	↓	↓	.10	↓	↓	81.3	↓	80.2	↓	81.1	78.8
55.21	.17	1.49	1.47	↓	↓	↓	↓	↓	81.3	↓	80.3	↓	81.1	78.9
60.12	↓	1.49	1.48	↓	↓	↓	83.0	↓	81.4	82.4	80.5	81.8	81.2	79.0
65.28	↓	1.49	1.45	↓	↓	↓	83.1	↓	↓	82.4	80.7	81.8	81.3	79.1
69.81	↓	1.48	1.45	↓	↓	↓	83.1	↓	↓	82.5	80.8	81.9	81.4	79.2
75.15	↓	1.48	1.45	-.02	↓	↓	83.2	↓	↓	82.5	81.0	81.9	81.5	79.2
81.01	↓	1.47	1.47	↓	↓	↓	83.2	↓	↓	82.5	81.2	82.0	81.6	79.3
85.37	.18	1.46	1.46	↓	↓	↓	83.4	83.2	↓	82.6	81.3	82.0	81.7	79.5
90.48	.17	1.46	1.46	↓	↓	↓	83.4	↓	↓	82.7	81.5	82.1	81.8	79.6
95.19	.17	1.45	1.46	-.03	.09	.09	83.5	↓	81.5	82.7	81.7	82.2	81.9	79.8
106.76	.03	.54	.36	-.09	-.55	.18	83.6	↓	81.4	82.8	82.1	82.3	82.1	80.0

Table III. Continued

Δtime	F_N	F_A	M_Y	M_X	M_Z	F_Y	T_1	T_2	T_3	T_4	T_5	T_6	T_7	T_8
Unpowered configuration: $M_\infty = 5.94$; $R_\infty = 2.10 \times 10^6/\text{ft}$; $\alpha = -3.47^\circ$; T_{ij} and p_{ij} not applicable														
0	-0.02	-0.01	-0.42	0.03	-0.88	0.14	86.4	86.0	87.6	85.9	83.9	85.5	81.9	83.4
13.93	-2.79	1.20	-7.54	-.16	.36	.13	↓	86.0	87.6	↓	83.9	85.5	81.9	↓
24.30	↓	1.01	-7.50	-.12	.35	.12	↓	86.0	87.6	↓	84.0	85.5	81.9	↓
30.46	↓	.97	-7.54	-.17	.37	↓	↓	85.9	87.5	↓	84.0	85.4	81.8	↓
34.07	↓	.95	-7.54	-.17	↓	↓	↓	86.0	87.5	↓	84.1	85.5	81.9	↓
38.93	-2.80	.93	-7.49	-.12	↓	↓	86.5	↓	87.6	↓	84.1	85.5	85.0	83.5
43.49	-2.79	.91	-7.50	-.17	↓	↓	86.6	↓	↓	86.0	84.6	85.6	85.1	83.6
48.15	-2.80	.90	-7.50	-.12	.35	↓	86.7	↓	↓	86.0	84.9	85.6	85.2	83.7
53.51	↓	.89	-7.51	-.17	.37	↓	86.8	86.1	↓	86.1	85.3	85.7	85.4	83.8
58.37	↓	.87	↓	-.12	.35	↓	86.9	86.1	↓	86.2	85.6	85.8	85.5	83.9
63.58	↓	.86	↓	-.13	.37	↓	87.0	86.0	↓	86.1	86.0	85.7	85.7	84.0
68.59	-2.82	.84	↓	-.18	.37	↓	87.2	↓	↓	86.2	86.1	85.8	85.9	84.2
73.50	-2.82	.83	-7.46	-.13	.37	↓	87.3	↓	↓	86.3	86.8	85.9	86.0	84.4
78.86	-2.83	.82	-7.51	↓	.38	.11	87.5	↓	↓	86.4	87.3	86.0	86.3	84.7
84.27	-2.83	.80	-7.51	↓	.35	.11	87.6	↓	↓	86.5	87.8	86.1	86.5	85.0
89.37	-2.81	.80	-7.52	↓	.37	.12	87.8	86.1	↓	86.7	88.3	86.3	86.8	85.3
94.18	-2.86	.79	-7.46	↓	.35	.11	88.0	↓	↓	86.8	88.7	86.5	87.0	85.6
98.59	-2.69	.78	-7.40	↓	.38	.09	88.2	↓	↓	86.9	89.2	86.6	87.3	85.9
103.70	-.11	-.81	-.38	.02	-.76	.11	88.5	↓	87.7	87.1	89.7	86.8	87.6	86.3
Unpowered configuration: $M_\infty = 5.93$; $R_\infty = 2.09 \times 10^6/\text{ft}$; $\alpha = -3.47^\circ$; T_{ij} and p_{ij} not applicable														
0	0.73	1.68	1.63	0.01	0.50	0.21	81.9	82.2	82.8	81.5	79.7	81.6	81.0	79.4
15.23	.50	2.13	2.39	.01	.51	.23	81.9	82.3	82.8	81.5	79.7	81.6	81.1	79.5
20.39	.50	2.33	2.39	.01	.51	↓	81.8	82.1	82.7	81.4	79.6	81.5	81.0	79.4
25.80	.53	2.23	2.40	.02	.55	↓	81.7	↓	↓	81.3	79.5	↓	80.9	79.3
30.56	.53	2.20	2.41	.01	.58	↓	81.8	↓	↓	81.3	79.5	↓	80.9	79.3
35.82	.51	2.18	2.36	.01	.59	.22	81.8	↓	↓	81.3	79.7	↓	81.0	79.4
39.98	.54	2.17	2.37	.03	.55	.25	81.9	↓	82.8	81.4	79.8	81.6	81.1	79.5
44.19	.54	2.17	2.38	.01	.59	.22	82.0	82.2	↓	81.5	79.9	81.6	81.2	79.5
49.90	.53	2.16	2.39	.02	.57	.21	82.0	82.2	↓	81.5	80.1	81.7	81.2	79.7
54.81	.71	1.34	1.44	.01	.30	.21	82.0	82.2	↓	81.5	80.2	81.7	81.3	79.8

Table III. Continued

Δtime	F_N	F_A	M_Y	M_X	M_Z	F_Y	T_1	T_2	T_3	T_4	T_5	T_6	T_7	T_8
Unpowered configuration; $M_\infty = 5.94$; $R_\infty = 2.12 \times 10^6/\text{ft}$; $\alpha = -4.89^\circ$; T_{ij} and p_{ij} not applicable														
0	0.08	-0.01	0.22	-0.08	-0.76	0.19	84.7	84.5	85.8	84.4	82.5	83.8	83.1	81.5
12.93	6.14	2.75	14.80	-.08	.45	.23	84.8	↓	85.8	84.4	82.5	↓	83.1	81.6
25.80	6.15	2.57	14.86	-.03	.45		84.8	↓	85.8	84.4	82.6	↓	83.2	↓
32.61	6.18	2.54	14.83	-.08	.43		84.8	↓	85.7	84.3	82.6	↓	↓	↓
38.02	6.20	2.53	14.92	-.03	.45		84.7	84.4	85.6	84.2	82.7	83.7	↓	↓
42.88	6.18	2.52	14.83	↓	↓		84.7	↓	85.6	84.2	82.8	83.7	↓	81.7
48.39	6.18	2.51	14.82	↓	↓		84.9	↓	85.7	84.4	83.0	83.8	83.5	81.9
53.05	6.17	2.51	14.89	↓	↓		84.9	↓	85.6	84.4	83.2	83.9	83.6	82.1
58.01	6.04	2.46	14.49	↓	.44	↓	85.0	84.5	85.7	84.5	83.5	84.0	83.8	82.3
62.32	5.98	2.43	14.34	↓	.46	.22	85.1	↓	↓	84.6	83.7	84.1	83.9	82.6
67.93	5.94	2.42	14.29	-.04	.44	.21	85.3	↓	↓	84.7	84.0	84.3	84.2	83.0
72.74	5.93	2.42	14.26	.01	.44	.21	85.3	↓	↓	84.8	84.3	84.4	84.4	83.3
78.15	5.91	2.42	14.24	-.04	.44	.21	85.4	↓	↓	84.9	84.6	84.6	84.6	83.7
82.96	5.90	2.41	14.22	↓	.43	.20	85.6	↓	↓	85.1	84.9	84.8	84.8	84.1
88.92	5.87	2.41	14.19	↓	.46	.20	85.7	↓	↓	85.3	85.3	85.0	85.1	84.6
93.93	5.86	2.41	14.17	↓	.45	.20	85.9	↓	↓	85.5	85.6	85.2	85.4	85.0
102.00	.01	.21	.24	-.08	-.80	.14	86.2	84.6	85.8	85.9	86.3	85.7	85.9	85.9
Unpowered configuration; $M_\infty = 6.02$; $R_\infty = 4.04 \times 10^6/\text{ft}$; $\alpha = -0.16^\circ$; T_{ij} and p_{ij} not applicable														
0	-0.06	0	0.49	-0.19	-0.90	0.08	84.2	85.8	86.5	83.5	80.5	83.5	82.7	79.9
14.03	.32	3.87	5.12	-.17	.81	.25	84.3	85.9	86.5	83.5	80.6	83.6	82.8	80.0
20.74	.33	3.70	5.00	-.17	.80	.25	84.2	85.8	86.5	83.5	80.6	83.5	82.8	80.0
25.75	.36	3.66	4.88	-.12	.82	.25	84.2	↓	86.1	83.4	80.7	83.5	82.8	80.0
30.66	.37	3.63	4.88	↓	.80	.26	84.3	↓	↓	83.5	80.8	83.6	82.9	80.1
35.62	.37	3.62	4.90	↓	.79	.25	84.4	↓	↓	83.5	81.0	83.6	83.0	80.2
40.48	.38	3.61	4.91	↓	.76	.24	84.4	↓	↓	83.6	81.3	83.7	83.1	80.4
45.54	.39	3.60	4.90	-.09	.77	.23	84.6	↓	86.5	83.7	81.6	83.8	83.4	80.8
50.50	.41	3.57	4.97	-.07	.78	.25	84.7	↓	↓	83.8	82.0	84.0	83.6	81.2
55.51	.39	3.56	4.86	-.07	.80	.26	84.8	85.9	↓	84.0	82.1	84.2	83.9	81.6
60.97	.43	3.57	4.88	-.04	↓	.24	85.1	↓	↓	84.2	82.9	84.5	84.2	82.2
65.98	.42	3.57	4.88	-.04	↓	.25	85.2	↓	↓	84.4	83.1	84.7	84.6	82.8
71.29	.43	3.58	4.78	-.02	↓	.28	85.4	↓	↓	84.7	83.9	85.0	85.0	83.5
77.10	.44	3.57	4.87	.01	.78	.25	85.7	↓	↓	85.0	84.6	85.4	85.4	84.1
81.41	.45	3.57	4.85	.01	.77	.24	85.9	86.0	86.6	85.3	85.1	85.8	85.8	85.1
85.87	.46	3.56	4.84	.01	.78	.23	86.2	86.1	86.6	85.6	85.6	86.2	86.3	85.9
90.43	↓	3.58	4.85	.06	.78	.24	86.5	86.1	86.7	86.0	86.2	86.6	86.7	86.7
95.69	↓	3.59	4.87	↓	.79	.23	86.8	86.2	86.7	86.4	86.9	87.1	87.2	87.7
100.65	↓	3.61	4.98	↓	.78	.24	87.2	86.3	86.8	86.9	87.6	87.6	87.7	88.7
105.01	.47	3.61	4.87	↓	.79	.23	87.4	86.1	86.8	87.2	88.2	88.0	88.2	89.5
110.47	.44	3.59	4.82	.05	.77	.22	87.7	86.3	86.7	87.6	88.9	88.5	88.7	90.6
115.68	.46	3.61	4.83	.05	.78	.20	87.9	86.3	86.7	88.0	89.5	88.9	89.1	91.6
120.54	.46	3.64	4.86	.10	.79	.19	88.3	86.1	86.8	88.5	90.3	89.5	89.7	92.6
125.60	.84	3.64	5.18	.06	.78	.20	88.7	86.5	86.8	89.0	91.1	90.1	90.3	93.7
131.71	.03	.53	.39	-.16	-.86	.12	89.1	86.5	86.8	89.6	91.8	90.7	90.8	95.0

Table III. Continued

Δtime	F_N	F_A	M_Y	M_X	M_Z	F_Y	T_1	T_2	T_3	T_4	T_5	T_6	T_7	T_8
Unpowered configuration: $M_\lambda = 6.01$; $R_\lambda = 7.47 \times 10^6/\text{ft}$; $\alpha = -3.49^\circ$; T_{ij} and p_{ij} not applicable														
0	0.09	-0.01	0.44	0.27	-1.17	0.06	85.4	91.1	88.8	84.1	80.2	86.3	85.2	80.4
13.43	-10.15	4.91	-26.07	-.07	1.15	.42	85.6	91.2	88.9	84.5	80.5	86.5	85.4	80.7
18.59	-10.15	4.60	-26.03	0	1.22	.43	85.6	91.2	88.9	84.6	80.6	86.5	85.5	80.7
23.30	-10.15	4.51	-26.05	.02	1.22	.43	85.6	91.1	88.8	84.5	80.6	86.5	85.4	80.7
27.86	-10.14	4.46	-26.06	0	1.10	.42	85.5	90.9	88.7	84.3	80.6	86.3	85.4	80.6
32.77	-10.14	4.42	-26.07	.09	1.20	.44	85.7	91.1	88.8	84.6	81.1	86.5	85.6	81.0
38.03	-10.13	4.39	-26.07	.09	1.15	.43	86.0	91.3	89.0	84.8	81.8	86.8	86.0	81.3
43.59	-10.12	4.36	-26.07	.09	1.20	.42	86.1	91.2	88.9	84.9	82.4	86.9	86.2	81.7
48.85	-10.11	4.33	-26.05	.19	1.20	.42	86.3	91.1	88.8	84.9	83.1	87.0	86.4	82.1
54.61	-10.09	4.31	-26.05	.09	1.10	.38	86.6			85.2	84.1	87.3	86.9	82.9
58.92	-10.10	4.29	-26.06	.16	1.13	.38	86.9			85.5	85.0	87.6	87.3	83.5
63.92	-10.09	4.28	-25.96	.23	1.17	.41	87.3			85.8	86.1	88.0	87.8	84.4
67.98	-10.07	4.27	-25.95	.35	1.10	.36	87.5	90.9	88.7	86.0	86.9	88.2	88.2	85.1
75.25	-10.08	4.26	-25.95	.21	1.13	.41	88.2	90.9	88.7	86.7	88.6	88.9	89.1	86.7
79.20		4.25	-25.96	.26	1.10	.39	88.8	91.2	88.9	87.4	89.9	89.6	89.9	87.9
83.71		4.25	-25.94	.35	1.20	.35	89.4	91.3	89.1	88.0	91.2	90.2	90.6	89.2
88.12		4.27	-25.94	.26	1.10	.33	90.0	91.4	89.2	88.7	92.5	90.8	91.4	90.4
92.93		4.25	-25.93	.31	1.10	.36	90.5			89.3	93.7	91.4	92.1	91.7
98.39			-25.94	.38	1.10	.34	91.2			90.0	95.3	92.1	92.9	93.3
104.75	-10.11		-25.93	.33	1.06	.30	91.9			90.8	97.1	93.0	94.0	95.2
109.51	-10.10		-25.94	.42	1.15	.29	92.6	91.5		91.6	98.4	93.7	94.7	96.6
114.87	-10.12		-25.94	.35	.98	.26	93.3	91.5	89.3	92.5	100.1	94.6	95.7	98.1
119.03	-10.13		-25.93	.37	.94	.30	93.8	91.5	89.3	93.1	101.3	95.2	96.4	99.7
123.69	-10.11		-25.92	.30	1.05	.26	94.5	91.6	89.4	93.9	102.7	96.0	97.3	101.2
133.06	.10	-.79	.31	.45	-1.05	-.08	95.9	91.8	89.5	95.6	105.6	97.6	99.1	104.4

Table III. Continued

Δtime	F_N	F_A	M_Y	M_X	M_Z	F_Y	T_1	T_2	T_3	T_4	T_5	T_6	T_7	T_8
Unpowered configuration; $M_\infty = 6.02$; $R_\infty = 7.40 \times 10^6/\text{ft}$; $\alpha = -0.15^\circ$; T_{ij} and p_{ij} not applicable														
0	0.02	-0.04	0.23	0.01	-1.21	0.10	86.9	91.2	89.6	86.1	82.9	88.0	87.2	83.7
19.84	.73	8.30	9.81	-.02	1.61	.43	86.9	91.0	89.5	86.0	82.9	87.9	87.1	83.7
26.30	.75	8.12	9.80	-.07	1.56	.45	86.9	91.0	89.4	86.0	83.0	87.9	87.2	83.8
32.81	.76	8.02	9.88	-.07	1.61	.47	86.8	90.8	89.2	85.8	83.2	87.8	87.1	83.7
38.38	.74	7.97	9.77	-.07	1.63	.43	87.1	91.0	89.4	86.0	83.9	88.0	87.5	84.0
43.03	.72	7.93	9.77	.02	1.74	.47	87.5	91.1	89.5	86.3	84.8	88.3	88.0	84.4
47.09	.74	7.89	9.87	0	1.60	.43	87.7	91.2	89.6	86.5	85.6	88.5	88.5	84.8
51.60	.76	7.85	9.88	.07	1.51	.47	88.0	91.2	89.6	86.6	86.5	88.6	89.0	85.1
57.16	.73	7.81	9.89	.05	1.65	.41	88.4	91.2	89.6	86.9	87.7	88.9	89.7	85.8
62.22	.75	7.78	9.80	.09	1.59	.42	88.7	91.1	89.4	87.2	88.9	89.2	90.5	86.5
67.43	.74	7.74	9.80	.14	1.56	.43	89.2	91.0	89.4	87.5	90.2	89.5	91.3	87.4
71.84	.77	7.72	9.86	.19	1.61	.43	89.7	91.1	89.4	87.9	91.5	90.0	92.2	88.4
76.40	.75	7.69	9.91	.05	1.63	.41	90.5	91.3	89.6	88.6	93.1	90.7	93.4	89.6
81.51	.74	7.68	9.95	.12	1.68	.39	91.2	91.4	89.7	89.3	94.7	91.4	94.5	90.9
85.97	.77	7.66	9.91	.16	1.63	.43	91.8	91.5	89.8	90.0	96.2	92.1	95.6	92.3
91.18	.77	7.64	10.01	.07	1.59	.38	92.6	91.7	89.9	90.8	97.9	92.8	96.9	93.8
96.04	.75	7.64	9.91	.05	1.49	.32	93.4	91.8	90.0	91.6	99.6	93.6	98.1	95.4
101.45	.75	7.62	10.01	.07	1.56	.39	94.3	92.0	90.2	92.6	101.4	94.6	99.6	97.2
106.66	.74	7.61	10.02	.05	1.54	.33	95.1	92.1	90.3	93.5	103.3	95.6	100.9	99.1
111.36	.71	7.60	10.00	.19	1.58	.33	95.9	92.3	90.4	94.4	104.9	96.5	102.2	100.8
117.18	.74	7.54	10.07	.09	1.30	.36	97.0	92.5	90.6	95.6	107.0	97.8	103.8	103.0
122.29	.73	7.28	10.04	.19	.30	.37	97.8	92.6	90.7	96.6	108.8	98.7	105.1	104.9
127.20	.74	6.67	10.02	.12	-2.17	.45	98.7	92.8	90.8	97.6	110.5	99.8	106.4	106.8
136.11	-.19	2.03	.19	-.01	-1.17	-.15	100.2	93.1	91.0	99.5	113.5	101.6	108.8	110.3

Table III. Continued

Δtime	F_N	F_A	M_Y	M_X	M_Z	F_Y	T_1	T_2	T_3	T_4	T_5	T_6	T_7	T_8
Unpowered configuration; $M_\infty = 6.01$; $R_\infty = 7.43 \times 10^6/\text{ft}$; $\alpha = 5.09^\circ$; T_{ij} and p_{ij} not applicable														
0	0.08	0	0.27	0.03	-0.78	0.08	87.5	93.3	90.4	86.7	83.0	89.1	88.0	83.7
11.57	22.70	8.02	57.51	-.49	1.36	.67	87.7	93.4	90.5	86.8	83.2	89.3	88.2	83.9
17.29	22.67	7.74	57.46	-.49	1.34	.63	87.5	93.2	90.3	86.5	83.0	89.0	88.0	83.7
22.04	22.68	7.64	57.41	-.54	1.39	.65	87.5	93.1		86.5	83.1	89.0	88.0	83.7
29.31	22.70	7.56	57.40	-.49	1.41	.65	87.6	93.1		86.6	83.6	89.0	88.1	83.8
36.97	22.72	7.50	57.37	-.40	1.38	.67	87.8	93.1		86.7	84.5	89.2	88.4	84.1
46.59	22.73	7.43	57.17	-.35	1.50	.64	88.5	93.3	90.4	87.1	86.5	89.6	89.3	85.1
53.10	22.75	7.38	57.14	-.35	1.45	.63	89.1	93.3	90.4	87.5	88.2	89.9	90.1	85.9
57.41	22.77	7.35	57.15	-.31	1.48	.66	89.6	93.4	90.5	87.9	89.4	90.3	90.6	86.7
61.77	22.74	7.32	56.94	-.28	1.38	.60	90.1	93.4	90.6	88.4	90.7	90.7	91.3	87.5
67.18	22.77	7.31	57.14	-.28	1.45	.58	90.8	93.5	90.7	89.0	92.5	91.3	92.2	88.7
71.39	22.76	7.28	56.93	-.30	1.48	.61	91.4	93.6	90.8	89.5	93.9	91.8	92.9	89.8
76.60	22.77	7.27	56.74	-.31	1.55	.66	92.0	93.5	90.7	90.1	95.6	92.3	93.6	90.9
81.16	22.73	7.24	56.69	-.28	1.43	.55	92.8	93.6	90.8	90.8	97.3	92.9	94.5	92.2
86.22	22.69	7.23	56.67	-.26	1.50	.64	93.6	93.7	90.9	91.7	99.2	93.6	95.5	93.8
91.78	22.74	7.21	56.66	-.30	1.31	.56	94.6	93.8	91.1	92.6	101.3	94.5	96.7	95.5
96.09	22.72	7.20	56.84	-.28	1.52	.56	95.3	93.9	91.1	93.4	102.9	95.2	97.5	96.9
101.10		7.20	57.02	-.21	1.36	.54	96.0	93.7	91.0	94.1	104.7	95.8	98.4	98.3
106.36		7.19	56.80	-.16	1.40	.59	96.8	93.6	90.9	95.0	106.5	96.5	99.3	100.0
111.57		7.18	56.79	-.19	1.36	.52	97.7	93.7	91.0	96.1	108.6	97.4	100.4	101.8
116.48	22.69	7.18	56.72	-.28	1.40	.54	98.4	93.6	90.9	96.9	110.3	98.2	101.3	103.5
122.14	22.69	7.18	56.92	-.12	1.38	.46	99.5	93.7	91.0	98.1	112.6	99.2	102.6	105.5
131.60	.04	.62	.30	.02	-.48	-.16	101.7	94.2	91.6	100.6	116.7	101.4	105.0	109.4
Powered configuration; jet off; $M_\infty = 5.82$; $R_\infty = 0.56 \times 10^6/\text{ft}$; $\alpha = -0.18^\circ$; T_{ij} and p_{ij} not applicable														
0	-0.02	0.04	0.15	0.22	-0.01	0.08	80.4	80.9	81.3	80.2	78.1	80.2	79.4	78.1
33.62	.25	1.16	5.06	-.17	.11	.07	80.4	80.8	81.2	80.1	78.1			
38.78	.25	1.13	5.06		.09	.06	80.5	80.9		80.2	78.2			
43.89	.25	1.11	3.59		.11	.07	80.4	80.8		80.2				
48.90	.24	1.10	5.08		.11	.07		80.8		80.1				
54.10	.25	1.09	5.10		.12	.06		80.7						
59.17	.24	1.08	5.13		.11	.07		80.8			78.3			
64.68		1.07	5.18		.12	.06		80.7			78.4			
69.73		1.06	5.17		.12	.06	80.5	80.8		80.2	78.5		79.5	
74.24		1.05	5.23		.12	.06	80.5			80.2	78.5		79.5	78.3
78.25	.23	1.05	5.25		.11	.07	80.6			80.2	78.6		79.6	78.2
83.96	.23	1.04	5.25	-.18	.12	.06	80.7			80.3	78.8	80.3	79.7	78.3
88.92	.29	1.03	5.38	-.17	.14	.07	80.7			80.2	78.8	80.3	79.7	78.3
94.18	-.06	.05	.15	.32	.02	.08	80.7		81.3	80.3	79.0	80.3	79.7	78.5

Table III. Continued

Δtime	F_N	F_A	M_Y	M_X	M_Z	F_Y	T_1	T_2	T_3	T_4	T_5	T_6	T_7	T_8
Powered configuration; jet off; $M_\infty = 5.80$; $R_\infty = 0.57 \times 10^6/\text{ft}$; $\alpha = 4.90^\circ$; T_{ij} and p_{ij} not applicable														
0	0.08	0.12	0.18	-0.08	0.03	0.18	82.4	81.8	82.3	82.5	81.3	82.3	81.7	81.4
37.12	1.87	.96	11.12		.03	.13	82.5		82.3		81.4	82.4	81.8	81.3
42.83	1.88	.94	11.14		.04	.12	82.5		82.3		81.5		81.8	81.4
48.49		.93	11.19			.12	82.6		82.4		81.5		81.8	81.4
51.90		.93	11.18			.14	82.6				81.6		81.9	81.5
56.76		.92	11.24			.14	82.6				81.6	82.5	81.9	81.5
62.22	1.89	.91	11.25		.03	.13	82.7			82.6	81.7		81.9	81.5
66.38	1.89	.90	11.31		.03	.13	82.7			82.6	81.8		82.0	81.6
71.24	1.90	.89	11.34		.02	.13	82.7			82.6	81.9		82.0	81.6
76.55	1.90	.89	11.39			.15	82.8	81.9	82.5	82.7	82.0	82.6	82.1	81.7
82.11	1.90	.88	11.38				82.9			82.7	82.1	82.6	82.2	81.8
87.22	1.92	.88	11.46				82.9			82.8	82.2	82.7	82.2	81.9
92.33	1.90	.88	11.48				83.0			82.8	82.4	82.7	82.3	82.0
96.39	1.92	.87	11.51				83.0			82.8	82.5	82.7	82.3	82.0
101.95	1.90		11.53	-0.09		.13	83.1			82.9	82.6	82.8	82.4	82.1
105.95	1.90		11.53	-0.08	.01	.14	83.2	82.0	82.6	83.0	82.7	82.9	82.5	82.3
111.46	1.90		11.54	-0.09	.02	.13		81.9	82.6		82.8		82.5	82.4
116.02	1.89	.86	11.56	-0.08	.01	.14			82.5		82.9		82.5	82.4
121.13	1.90	.86	11.58	-0.09	.02	.13			82.5		83.0		82.6	82.5
126.09	1.90	.86	11.63	-0.09	.01	.14	83.3		82.5	83.1	83.1	83.0	82.6	82.6
133.96	.03	-.15	.27	-.10	.10	.19	83.4		82.6	83.2	83.3	83.0	82.7	82.8

Table III. Continued

Δt	F_N	F_A	M_Y	M_X	M_Z	F_Y	T_1	T_2	T_3	T_4	T_5	T_6	T_7	T_8
Powered configuration; jet off; $M_\infty = 6.02$; $R_\infty = 7.35 \times 10^6/\text{ft}$; $\alpha = -0.04^\circ$; T_{lj} and p_{lj} not applicable														
0	0.14	0.02	0.41	0.37	-0.87	0.18	82.3	83.3	83.4	82.1	79.8	82.3	81.6	80.2
12.33	4.33	9.49	81.13	-.82	.94	.96	82.4	83.3	↓	82.0	79.9	↓	81.6	80.3
18.84	4.35	9.18	81.16	-.82	.94	.95	82.5	83.3	↓	82.0	79.9	↓	81.6	80.2
23.70	4.34	9.08	81.15	-.72	1.00	.94	82.5	83.2	↓	82.0	80.1	↓	81.7	80.2
28.21	4.38	9.01	81.04	-.84	.91	.88	82.6	83.3	↓	82.1	80.5	82.4	81.8	80.3
33.59	4.38	8.91	81.06	-.74	1.05	.87	82.7	↓	↓	82.1	81.3	82.5	82.1	80.5
38.08	4.39	8.84	81.11	-.81	1.11	.92	83.0	↓	83.5	82.2	82.2	82.6	82.5	80.7
43.09	4.39	8.76	81.11	-.63	1.02	.90	83.3	↓	↓	82.3	83.3	82.7	82.9	81.0
48.24	4.40	8.69	80.96	-.69	1.11	.84	83.8	↓	↓	82.6	84.7	82.9	83.7	81.5
53.35	4.39	8.63	80.83	-.69	.99	.87	84.2	↓	↓	82.8	86.1	83.1	84.5	82.1
59.17	4.40	8.54	81.03	-.48	.90	.82	84.8	83.2	83.4	83.1	87.8	83.5	85.4	82.8
64.08	4.41	7.74	80.89	-.69	-1.75	1.03	85.4	83.2	83.4	83.5	89.5	83.9	86.4	83.6
68.58	4.40	6.45	81.12	-.67	-6.17	1.22	86.0	83.2	83.5	83.9	91.0	84.3	87.3	84.5
73.04	4.41	5.44	81.15	-.62	-9.52	1.41	86.7	83.4	83.6	84.4	92.6	84.8	88.4	85.5
78.55	4.36	4.58	81.41	-.59	-12.36	1.57	87.6	83.4	83.6	85.0	94.6	85.4	89.6	86.7
82.86	4.38	3.98	81.49	-.59	-14.20	1.60	88.3	83.5	83.7	85.6	96.2	86.0	90.7	87.8
88.07	4.32	3.44	81.78	-.66	-16.07	1.72	89.1	83.6	86.8	86.3	98.1	86.7	92.0	89.1
93.33	4.57	2.91	82.19	-.59	-17.74	1.83	90.0	83.7	83.8	87.0	100.1	87.5	93.3	90.5
98.09	-.19	-.54	.61	.42	-.92	.04	90.8	83.7	83.8	87.7	101.6	88.1	94.4	91.8
Powered configuration; jet off; $M_\infty = 6.00$; $R_\infty = 7.35 \times 10^6/\text{ft}$; $\alpha = 5.06^\circ$; T_{lj} and p_{lj} not applicable														
0	0.12	-0.01	0.42	-0.26	-1.41	0.13	79.6	82.0	81.8	79.0	75.9	79.0	78.2	74.9
7.72	27.08	11.93	170.61	-1.34	1.39	1.11	79.6	82.0	81.7	78.9	75.9	79.0	↓	↓
13.18	27.16	11.71	170.97	-1.32	1.32	1.07	79.7	82.0	81.7	78.9	75.9	79.1	↓	↓
18.59	27.20	11.56	171.12	-1.32	1.27	1.07	↓	81.9	81.7	78.8	76.0	79.1	↓	↓
22.74	27.25	11.55	171.12	-1.22	1.15	1.02	↓	81.9	81.6	78.8	76.1	79.0	↓	↓
27.35	27.30	11.42	171.29	-1.22	1.27	1.04	↓	81.8	81.6	78.8	76.5	↓	78.3	↓
32.56	27.34	11.34	171.09	-1.20	1.15	1.00	79.8	81.7	81.5	78.7	77.1	↓	78.4	75.0
37.02	27.35	11.29	171.16	-1.20	1.22	1.00	79.9	81.7	81.5	78.8	77.8	↓	78.6	75.2
42.33	27.30	11.23	170.85	-1.22	1.36	1.06	80.2	81.7	81.4	79.0	78.8	79.2	79.0	75.5
47.39	27.32	10.77	171.13	-1.13	-.33	1.04	80.6	81.6	81.4	79.1	80.0	79.3	79.5	75.9
52.35	27.27	9.31	171.14	-1.10	-5.38	1.34	81.0	81.7	81.5	79.3	81.2	79.6	80.1	76.5
57.16	27.21	8.12	171.18	-1.10	-9.36	1.56	81.5	81.6	81.4	79.6	82.6	79.8	80.7	77.1
62.17	27.16	7.04	171.36	-1.06	-13.06	1.70	82.1	81.6	81.5	80.0	84.1	80.2	81.4	77.9
67.53	27.17	6.24	171.51	-1.06	-15.31	1.87	82.8	81.8	81.6	80.6	85.9	80.8	82.3	78.9
72.44	27.18	5.67	171.48	-1.03	-16.90	1.96	83.7	82.0	81.8	81.2	87.7	81.3	83.3	80.0
78.00	27.16	5.48	171.89	-1.01	-17.49	1.91	84.4	82.0	81.8	81.7	89.5	81.9	84.2	81.0
86.67	-.08	-.49	.33	-.34	-.85	.03	85.7	82.0	81.9	82.7	92.4	82.8	85.8	82.9

Table III. Continued

Δt_{time}	F_N	F_A	M_Y	M_X	M_Z	F_Y	T_1	T_2	T_3	T_4	T_5	T_6	T_7	T_8	T_{ij}	p_{tj}
Powered configuration; cold-air exhaust gas; $M_\infty = 5.82$; $R_\infty = 0.61 \times 10^6/\text{ft}$; $\alpha = -0.12^\circ$																
0	-0.06	-0.19	0.25	-0.28	-1.25	0.05	84.8	85.5	86.0	84.6	82.1	84.6	83.8	82.2	80.8	0.38
49.79	3.20	-22.90	38.68	-.07	3.01	-.47	85.3	85.2	86.1	84.7	82.4	84.5	83.7	81.9	78.1	18.52
59.36	3.09	-22.13	37.59	.01	2.86	-.44	85.3	85.5	↓	84.8	82.5	84.7	84.0	82.1	84.5	18.84
64.72	3.23	-23.27	39.20	.09	3.02	-.46	85.3	86.0		84.9	82.6	84.9	84.4	82.2	87.1	19.83
69.18	3.19	-23.10	39.01	.10	2.99	-.44	85.4	86.5	↓	85.0	82.8	85.2	84.8	82.4	88.6	19.71
74.59	3.19	-23.07	38.97	.19	2.97	-.47	85.6	87.1		85.1	82.9	85.6	85.3	82.6	90.0	19.68
79.20	3.18	-23.03	38.94	.24	2.99	-.42	85.7	87.6	86.3	85.3	83.2	86.0	85.8	82.9	91.1	19.65
84.66	3.16	-23.05	38.97	.28	2.99	-.44	85.9	88.2	86.3	85.5	83.6	86.5	86.4	83.2	92.0	19.66
89.22	3.16	-23.05	38.97	.29	3.01	-.40	86.2	88.8	86.4	85.8	83.9	87.0	86.9	83.6	92.7	19.65
94.68	3.16	-23.01	38.93	.43	3.01	-.38	86.5	89.4	86.6	86.1	84.4	87.5	87.6	84.1	93.5	19.62
99.44	3.15	-23.04	38.99	.47	3.04	-.41	86.7	89.8	86.6	86.4	84.8	88.0	88.2	84.5	94.0	19.64
104.04	3.14	-23.11	39.10	.37	3.01	-.41	86.9	90.3	86.7	86.6	85.3	88.5	88.7	85.0	94.5	19.68
109.66	3.16	-23.13	39.20	.37	3.01	-.42	87.3	90.9	86.9	87.0	85.9	89.2	89.5	85.6	95.1	19.67
114.27	3.14	-23.02	39.02	.51	2.97	-.40	87.7	91.4	87.1	87.3	86.5	89.7	90.1	86.2	95.5	19.60
119.78	3.14	-23.08	39.16	.65	2.99	-.39	88.1	92.0	87.3	87.8	87.1	90.4	90.9	86.9	95.9	19.64
124.23	3.14	-23.13	39.25	.50	3.01	-.43	88.5	92.4	87.5	88.1	87.6	90.9	91.4	87.4	96.2	19.67
129.59	.30	.85	6.25	.41	.08	.15	88.5	92.8	87.7	88.3	88.3	91.0	91.6	88.0	94.9	7.56
135.41	-.07	.16	.22	-.31	-.43	.18	88.8	92.9	87.9	88.7	88.9	91.4	91.7	88.5	98.1	2.34
Powered configuration; cold-air exhaust gas; $M_\infty = 5.79$; $R_\infty = 0.60 \times 10^6/\text{ft}$; $\alpha = 4.99^\circ$																
0	0.07	0.14	-0.09	0.37	0.27	0.18	83.8	87.2	86.2	83.2	79.7	83.6	82.6	78.8	77.8	0.13
16.03	4.54	-21.23	42.52	-.01	2.66	-.40	84.0	86.9	86.2	83.5	79.9	83.7	82.7	79.0	78.4	18.44
20.74	4.79	-23.22	45.48	.03	2.90	-.45	84.0	86.9	86.1	83.5	79.9	83.7	82.7	79.0	82.7	19.02
26.25	4.82	-23.55	45.97	.10	2.96	-.45	84.1	87.2	↓	83.6	80.0	83.9	83.0	79.2	86.4	19.92
30.71	4.77	-23.07	45.39	.16	2.94	-.44	84.2	87.6		83.7	80.1	84.1	83.3	79.3	88.5	19.55
36.17	4.81	-23.37	45.89	.19	2.97	-.45	84.4	88.2	↓	83.8	80.3	84.4	83.7	79.5	90.4	19.59
40.83	4.80	-23.47	46.10	.28	3.00	-.45	84.6	88.7		86.2	84.0	80.6	84.8	84.3	79.9	19.87
46.19	4.79	-23.31	45.90	.33	2.98	-.44	84.8	89.3	86.3	84.2	81.0	85.3	84.9	80.3	92.7	19.66
50.85	4.79	-23.32	45.96	.33	3.02	-.44	85.0	89.9	86.3	84.5	81.4	85.8	85.5	80.7	93.6	19.71
55.71	4.80	-23.35	46.07	.37	3.00	-.43	85.3	90.5	86.4	84.7	81.9	86.4	86.2	81.2	94.3	19.72
61.17	4.79	-23.25	45.96	.42	2.98	-.42	85.6	91.1	86.6	85.1	82.5	87.1	87.0	81.9	95.0	19.64
66.38	4.80	-23.39	46.22	.46	3.02	-.42	86.0	91.6	86.7	85.5	83.2	87.7	87.7	82.6	95.6	19.73
71.24	4.79	-23.35	46.18	.46	3.00	-.41	86.4	92.2	86.9	85.9	83.8	88.4	88.4	83.3	96.2	19.70
75.75	4.77	-23.37	46.21	.51	3.02	-.40	86.8	92.6	87.0	86.4	84.5	89.0	89.1	83.9	96.6	19.71
81.21	4.76	-23.37	46.17	.51	3.05	-.40	87.4	93.2	87.3	86.9	85.3	89.7	89.9	84.7	97.0	19.72
85.77	4.75	-23.34	46.17	.55	3.02	-.40	87.7	93.6	87.4	87.3	85.9	90.3	90.5	85.4	97.3	19.68
91.13	4.76	-23.36	46.18	.55	3.04	-.39	88.3	94.1	87.7	87.8	86.7	91.0	91.3	86.2	97.7	19.68
95.79	2.00	.30	13.25	.53	.26	.13	88.3	94.5	87.8	87.8	87.3	91.0	91.3	86.8	95.5	8.58
101.25	.02	-.16	.01	.42	.13	.14	88.5	94.5	88.0	88.3	88.0	91.4	91.5	87.4	99.3	2.60

Table III. Continued

Δtime	F_N	F_A	M_Y	M_X	M_Z	F_Y	T_1	T_2	T_3	T_4	T_5	T_6	T_7	T_8	T_{ij}	p_{ij}
Powered configuration; cold-air exhaust gas; $M_\infty = 6.02$; $R_\infty = 7.32 \times 10^6/\text{ft}$; $\alpha = 0.08^\circ$																
0	0.03	0	0.47	0.11	-0.77	0.13	84.1	88.4	87.0	83.5	79.5	84.0	82.9	78.8	77.9	0.33
15.33	7.00	-13.11	115.08	-.68	3.73	.37	84.4	88.3	87.0	83.8	79.8	84.2	83.1	79.0	83.8	18.51
19.94	7.18	-14.80	117.39	-.61	3.92	.37	84.7	88.6	87.1	84.0	80.2	84.5	83.5	79.3	88.0	18.82
25.40	7.27	-15.66	118.49	-.54	3.98	.34	84.9	89.1	87.0	84.2	80.8	84.7	84.0	79.5	91.2	20.09
30.01	7.20	-15.23	117.75	-.47	3.86	.33	85.3	89.6	87.1	84.4	81.6	85.0	84.8	79.9	93.4	19.71
35.67	7.16	-14.74	116.81	-.37	4.07	.40	85.8	90.3	87.1	84.7	82.9	85.6	85.8	80.4	95.3	19.26
40.53	7.27	-15.98	118.43	-.30	4.02	.34	86.5	91.0	87.3	85.2	84.3	86.3	87.0	81.1	96.7	20.05
45.14	7.19	-15.64	117.89	-.28	4.09	.36	87.0	91.4	87.2	85.5	85.6	86.9	88.0	81.8	97.6	19.91
50.65	7.12	-15.19	116.96	-.19	3.97	.33	87.7	92.1	87.3	86.0	87.3	87.7	89.5	82.8	98.6	19.47
54.96	7.19	-15.78	117.56	-.16	4.13	.34	88.6	92.7	87.5	86.7	88.9	88.5	91.0	83.9	99.5	19.84
60.52	7.12	-15.66	117.07	-.09	4.15	.37	89.7	93.5	87.8	87.6	91.0	89.7	92.8	85.4	100.4	19.73
65.53	7.12	-15.65	117.08	-.05	4.23	.36	90.7	94.1	88.0	88.4	92.8	90.7	94.4	86.8	101.0	19.70
70.44	7.11	-15.79	117.21	0	4.16	.35	91.8	94.9	88.4	89.4	94.8	92.0	96.1	88.3	101.7	19.73
74.85	7.11	-15.76	117.03	.07	4.06	.33	92.9	95.6	88.8	90.4	96.6	93.1	97.7	89.9	102.4	19.68
80.26	7.10	-15.81	116.97	.02	4.27	.44	94.2	96.4	89.3	91.5	98.7	94.4	99.5	91.7	103.1	19.70
84.87	7.10	-15.86	116.95	.14	4.13	.34	95.3	97.1	89.7	92.6	100.5	95.6	101.1	93.3	103.6	19.73
90.33	7.07	-15.90	116.78	.18	4.12	.33	96.4	97.8	90.1	93.7	102.3	96.9	102.8	95.1	104.0	19.72
94.89	7.08	-15.89	116.93	.18	4.19	.37	97.3	98.3	90.4	94.7	103.9	98.0	104.1	96.6	104.9	19.69
100.75	-.16	-.34	.63	.61	-.21	.09	97.6	98.7	90.6	95.5	105.7	98.6	104.7	98.3	107.9	5.42
Powered configuration; cold-air exhaust gas; $M_\infty = 6.02$; $R_\infty = 7.36 \times 10^6/\text{ft}$; $\alpha = 5.22^\circ$																
0	0.22	-0.04	-0.48	-0.19	-0.88	0.06	85.6	90.4	89.8	84.5	79.5	84.9	83.6	78.6	78.1	0.36
21.19	30.02	-10.50	206.76	-.86	4.75	.45	85.7	90.4	89.5	84.9	80.1	85.1	84.0	79.0	88.9	19.09
25.65	30.00	-10.19	206.11	-.77	4.57	.43	85.9	90.6	89.4	84.8	80.4	85.2	84.4	79.1	91.6	18.79
31.11	30.24	-12.39	209.00	-.68	4.80	.38	86.2	91.2	89.3	85.0	81.2	85.6	85.0	79.5	94.1	20.54
35.57	30.02	-10.84	206.81	-.61	4.82	.42	86.6	91.6	89.3	85.3	82.1	85.9	85.7	79.9	95.5	19.48
41.08	29.93	-10.31	205.56	-.54	4.66	.42	87.1	92.3	89.3	85.6	83.4	86.6	86.8	80.7	97.1	18.76
45.64	30.14	-12.32	208.09	-.49	4.86	.40	87.9	93.1	89.6	86.4	84.9	87.5	88.1	81.8	98.4	20.33
50.70	30.05	-11.87	207.46	-.47	4.91	.41	88.7	93.9	89.9	87.1	86.6	88.5	89.5	82.9	99.6	19.97
55.96	29.92	-11.45	206.31	-.35	4.77	.39	89.3	94.4	89.9	87.6	88.1	89.3	90.8	84.0	100.3	19.57
60.67	29.83	-11.07	205.05	-.37	4.76	.43	90.1	95.0	90.1	88.3	89.6	90.2	92.0	85.3	101.0	19.23
66.23	29.95	-12.22	206.56	-.37	4.83	.43	91.2	95.8	90.4	89.4	91.7	91.5	93.8	86.9	101.8	20.09
70.74	29.84	-11.85	205.74	-.35	4.99	.46	92.0	96.4	90.7	90.2	93.4	92.4	95.1	88.3	102.4	19.79
75.65	29.82	-11.67	205.41	-.28	5.01	.46	93.0	97.1	91.0	91.2	95.1	93.5	96.6	89.8	103.0	19.55
81.06	29.78	-11.89	205.63	-.14	4.71	.36	93.8	97.5	91.1	92.0	96.8	94.4	98.0	91.2	103.2	19.76
85.72	29.89	-12.06	205.64		4.95	.36	94.5	97.8	91.2	92.7	98.3	95.3	99.1	92.5	103.4	19.79
92.83	29.71	-11.99	204.96		4.74	.37	95.8	98.6	91.5	94.1	100.7	96.8	101.0	94.6	103.7	19.72
96.34	29.66	-12.01	205.09		4.81	.37	96.5	98.9	91.7	94.7	101.8	97.5	101.8	95.6	103.9	19.73
110.27	.04	.64	.59	-.23	-.46	-.06	98.3	99.2	92.4	96.9	106.3	99.3	103.4	99.3	113.4	2.06

Table III. Continued

Δt_{time}	F_N	F_A	M_Y	M_X	M_Z	F_Y	T_1	T_2	T_3	T_4	T_5	T_6	T_7	T_8	T_{ij}	p_{ij}
Powered configuration; hot-air exhaust gas; $M_\infty = 5.78$; $R_\infty = 0.61 \times 10^6/\text{ft}$; $\alpha = -0.07^\circ$																
0	0.07	0.11	0.20	-0.06	0.14	-0.17	84.8	84.5	85.7	84.6	82.5	84.1	83.4	82.2	82.0	0.19
17.89	3.06	-23.92	39.67	-.06	2.61	-.40	85.0	84.0	85.5	84.6	82.4	84.1	83.3	82.1	75.0	19.95
22.60	3.05	-23.68	39.29	.04	2.67	-.38	85.1	84.1	85.6	84.7	82.6	84.2	83.5	82.2	78.9	19.71
28.11	3.04	-23.59	39.25	.09	2.67	-.40	85.2	84.5	85.7	84.8	82.7	84.3	83.6	82.3	83.9	19.65
33.07		-23.54	39.21	.26	2.79	-.43	85.4	85.1	85.8	85.0	82.8	84.6	84.0	82.5	88.5	19.59
38.08		-23.57	39.27	.22	2.79	-.41	85.5	85.9		85.2	82.8	84.8	84.4	82.6	93.2	19.64
42.54		-23.49	39.17	.18	2.74	-.40	85.6	86.7		85.3	82.9	85.1	84.9	82.7	97.6	19.58
48.00		-23.52	39.21	.31	2.79	-.41	85.7	87.9		85.6	83.1	85.8	85.7	83.0	102.9	19.61
52.65		-23.56	39.27	.53	2.94	-.43	86.0	89.2	86.0	85.9	83.5	86.5	86.5	83.5	107.7	19.61
57.51		-23.59	39.36	.47	2.95	-.47	86.3	90.6	86.1	86.3	84.0	87.3	87.5	84.0	112.6	19.64
63.03		-23.54	39.27	.62	2.95	-.42	86.6	92.4	86.1	86.7	84.7	88.4	88.7	84.7	118.0	19.58
67.78	3.05	-23.60	39.32	.70	3.01	-.44	87.0	94.1	86.4	87.4	85.5	89.6	90.0	85.6	122.9	19.60
72.49	3.04	-23.55	39.27	.74	3.01	-.46	87.5	95.9	86.6	87.9	86.3	90.8	91.4	86.5	127.5	19.57
77.90	3.04	-23.63	39.34	.89	3.08	-.41	88.3	98.2	87.0	88.7	87.6	92.5	93.2	87.9	132.9	19.60
82.61	3.06	-23.75	39.52	.92	3.09	-.42	88.9	100.3	87.3	89.5	88.8	94.1	94.9	89.1	137.5	19.67
88.07	3.06	-23.71	39.47	1.23	3.18	-.44	89.8	102.9	87.8	90.7	90.4	96.2	97.1	90.8	142.8	19.64
92.58	3.05	-23.66	39.39	1.24	3.14	-.42	90.5	104.9	88.1	91.5	91.7	97.8	98.9	92.3	146.9	19.59
98.04	3.06	-23.75	39.50	1.28	3.20	-.43	91.5	107.5	88.6	92.6	93.4	100.0	101.1	94.2	151.8	19.63
103.40	3.07	-23.79	39.54	1.41	3.21	-.44	92.5	110.2	89.1	93.7	95.4	102.4	103.5	96.3	156.6	19.64
108.11	3.04	-23.77	39.46	1.53	3.25	-.47	93.8	112.6	89.6	94.6	97.0	104.3	105.6	98.1	160.6	19.60
115.68	-.26	-.49	.37	.76	.21	.08	95.0	116.2	90.4	95.7	100.2	106.7	107.4	101.1	156.7	6.13
Powered configuration; hot-air exhaust gas; $M_\infty = 5.79$; $R_\infty = 0.60 \times 10^6/\text{ft}$; $\alpha = 5.03^\circ$																
0	-0.10	-0.02	0.31	0.47	-0.93	0.11	86.6	86.1	88.8	86.0	82.9	84.9	84.1	82.3	81.9	0.08
16.18	4.68	-24.33	47.01	.07	2.73	-.47	87.1	86.7	88.9	86.4	83.2	85.4	84.8	82.6	97.0	20.44
20.89	4.60	-23.63	45.99	.18	2.79	-.51	87.1	87.9	88.8	86.5	83.3	85.7	85.3	82.8	108.4	19.93
25.65	4.52	-22.99	45.09	.34	2.80	-.52	87.2	89.6	88.8	86.5	83.3	86.1	85.9	82.9	117.3	19.42
31.31	4.45	-22.35	44.18	.49	2.86	-.54	87.4	92.2	88.8	86.7	83.7	87.2	87.2	83.5	125.6	18.89
36.22	4.61	-23.79	46.28	.60	3.05	-.57	87.7	94.6	88.9	87.1	84.2	88.5	88.7	84.2	132.6	20.00
40.73	4.57	-23.53	45.92	.75	3.09	-.57	88.2	97.0	89.1	87.5	85.0	89.9	90.2	85.0	138.1	19.82
45.99	4.56	-23.44	45.76	.88	3.13	-.58	88.7	99.8	89.3	88.1	86.2	91.7	92.2	86.3	143.9	19.68
50.70	4.54	-23.33	45.60	1.02	3.18	-.59	89.4	102.5	89.5	88.7	87.5	93.5	94.3	87.7	148.8	19.59
56.11	4.57	-23.45	45.78	1.15	3.22	-.59	90.2	105.5	89.9	89.7	89.2	96.0	96.5	89.5	154.1	19.63
60.92	4.54	-23.37	45.64	1.28	3.27	-.60	91.1	108.2	90.3	90.5	90.9	98.1	98.9	91.3	158.7	19.58
65.68	4.57	-23.48	45.77	1.41	3.30	-.60	92.1	110.9	90.7	91.6	92.8	100.3	101.2	93.3	163.0	19.61
71.24	4.57	-23.53	45.86	1.54	3.32	-.61	93.4	114.1	91.3	93.0	95.2	103.0	104.2	95.7	167.9	19.61
75.65	4.55	-23.72	45.83	1.63	3.36	-.61	94.6	116.7	91.8	94.1	97.2	105.4	106.6	97.9	171.6	19.59
86.17	4.55	-23.71	46.09	1.89	3.42	-.61	97.6	122.9	93.2	97.0	102.3	111.0	112.4	103.2	180.2	19.67
91.18	4.54	-23.73	46.10	2.02		-.62	99.1	125.8	93.9	98.4	104.9	113.8	115.3	105.8	184.0	19.66
96.24	4.51	-23.70	46.02	2.15		-.66	100.6	128.7	94.9	99.9	107.4	116.4	118.4	108.5	187.7	19.60
100.85	4.52	-23.80	46.12	2.23		-.66	102.0	131.4	95.3	101.3	109.9	119.0	121.1	111.1	191.1	19.64
106.16	4.51	-23.78	46.10	2.37	3.51	-.65	103.8	134.4	96.2	103.0	112.6	121.8	124.2	114.0	194.7	19.61
111.07	4.31	-22.23	43.88	2.49	3.34	-.61	105.3	137.2	97.0	104.8	115.3	124.6	127.1	116.8	197.4	19.30
117.53	-.10	-.72	.28	1.54	-.23	.04	106.8	138.8	98.1	106.8	119.3	126.9	127.3	120.0	189.2	3.30

Table III. Continued

Δt	F_N	F_A	M_Y	M_X	M_Z	F_Y	T_1	T_2	T_3	T_4	T_5	T_6	T_7	T_8	T_{tj}	p_{tj}
Powered configuration; hot-air exhaust gas; $M_\infty = 6.01$; $R_\infty = 7.39 \times 10^6/\text{ft}$; $\alpha = 0.06^\circ$																
0	0.04	-0.05	0.49	0.38	-0.78	0.14	92.7	95.5	95.7	91.9	88.0	91.8	90.7	87.2	86.7	0.34
15.43	7.28	-14.51	117.15	-.58	3.95	.35	93.1	96.1	95.7	92.3	88.3	92.2	91.3	87.5	110.7	19.34
20.04	7.23	-13.91	116.28	-.35	3.86	.31	93.2	97.3	95.6	92.3	88.5	92.4	91.9	87.6	122.5	18.89
24.85	7.43	-15.57	118.64	-.14	4.23	.32	93.6	99.3	95.7	92.7	89.1	93.2	93.0	88.0	132.9	19.88
30.21	7.37	-15.07	117.61	.09	4.23	.32	94.1	101.8	95.8	93.1	90.2	94.5	94.4	88.8	141.6	19.70
34.87	7.37	-15.27	117.50	.23	4.13	.30	94.7	104.4	95.9	93.6	91.5	96.9	95.3	90.0	147.7	19.77
40.33	7.39	-15.28	117.42	.51	4.27	.37	96.0	107.4	96.2	94.6	93.7	98.6	98.3	91.5	153.6	19.67
45.39	7.35	-15.35	117.31	.70	4.47	.36	97.4	110.4	96.6	95.8	96.2	100.2	101.7	93.1	158.5	19.70
49.80	7.30	-15.40	117.14	.86	4.40	.31	98.6	112.9	97.0	96.9	98.6	101.9	104.9	94.7	162.4	19.65
55.36	7.28	-15.48	117.16	1.05	4.47	.31	100.4	116.1	97.5	98.5	101.9	104.5	108.8	97.3	167.1	19.63
60.47	7.21	-15.60	116.72	1.16	4.70	.42	102.3	119.1	98.2	100.1	105.3	107.3	112.5	100.0	171.3	19.64
65.33	7.22	-15.68	116.84	1.32	4.70	.39	104.0	121.9	98.7	101.5	108.4	110.0	115.8	102.7	175.0	19.63
69.89	7.17	-15.81	116.78	1.49	4.55	.29	105.8	124.5	99.4	103.0	111.6	112.7	119.0	105.6	178.2	19.65
75.20	7.17	-15.87	116.85	1.63	4.56	.33	107.9	127.5	100.2	104.9	115.2	116.0	122.8	109.1	181.8	19.61
80.56	7.19	-15.90	116.91	1.76	4.62	.39	110.0	130.5	100.9	106.8	118.8	119.2	126.6	112.6	185.4	19.59
85.12	7.19	-16.00	116.89	1.90	4.57	.38	111.7	132.9	101.7	108.7	121.9	122.1	129.7	115.7	188.4	19.60
89.88	7.19	-16.05	116.91	2.06	4.43	.36	113.4	135.7	102.5	110.6	125.2	125.3	133.2	119.1	191.7	19.60
95.33	7.17	-16.16	116.95	2.13	4.45	.45	115.2	138.6	103.4	112.7	128.7	128.8	136.9	123.0	195.2	19.64
99.89	7.16	-16.21	117.02	2.32	4.38	.42	116.9	141.1	104.1	114.5	131.6	131.6	140.2	126.2	198.0	19.67
104.90	7.16	-16.31	117.14	2.43	4.40	.44	119.0	143.9	105.1	116.7	135.0	134.8	143.8	129.8	201.2	19.70
109.86	.55	1.50	17.11	1.61	-.44	.27	120.2	146.1	105.8	118.4	138.4	137.2	144.5	133.1	197.2	6.16
113.82	-.11	-1.01	.01	2.03	.04	.04	121.5	146.1	106.5	120.1	141.1	139.3	145.4	135.6	196.3	3.05
117.93	-.11	-1.02	1.00	2.04	-1.24	.01	123.0	145.5	107.2	121.8	143.7	141.2	146.9	138.2	194.3	1.95

Table III. Continued

Δtime	F_N	F_A	M_Y	M_X	M_Z	F_Y	T_1	T_2	T_3	T_4	T_5	T_6	T_7	T_8	T_{lj}	p_{lj}
Powered configuration; hot-air exhaust gas; $M_\infty = 6.01$; $R_\infty = 7.38 \times 10^6/\text{ft}$; $\alpha = 5.01^\circ$																
0	0.13	0	0.29	0.34	-0.84	0.21	89.2	88.4	90.6	89.0	86.3	88.0	87.1	86.1	85.9	0.34
16.63	29.09	-13.90	205.63	-.73	4.36	.50	89.9	89.7	90.7	89.5	86.7	88.7	88.3	86.6	108.1	20.59
21.54	29.04	-12.23	203.85	-.49	4.22	.52	90.1	91.4	90.8	89.6	87.0	89.2	89.1	86.9	118.6	19.25
26.60	28.73	-11.68	201.93	-.37	4.24	.49	90.3	93.5	90.8	89.7	87.5	89.9	90.3	87.2	126.9	18.67
31.56	29.01	-13.74	204.93	-.16	4.71	.44	90.7	95.9	90.9	90.1	88.5	91.1	92.1	87.9	134.7	20.15
36.37	28.95	-13.41	204.18	-.02	4.54	.45	91.4	98.4	91.1	90.5	89.8	92.5	94.2	88.9	141.1	19.92
41.18	28.85	-13.00	202.97	.05	4.60	.43	91.9	101.0	91.2	91.1	91.4	94.1	96.3	90.0	146.5	19.54
45.94	28.89	-13.33	203.52	.16	4.81	.46	92.6	103.5	91.4	91.7	93.2	95.8	98.6	91.4	151.6	19.68
51.35	28.85	-13.29	202.98	.42	4.90	.51	93.8	106.4	91.7	92.8	95.7	98.2	101.5	93.5	157.1	19.61
55.96	28.85	-13.46	202.87	.51	4.88	.40	94.9	109.0	92.1	93.8	98.0	100.3	104.3	95.5	161.6	19.68
61.47	28.83	-13.54	202.52	.63	5.01	.41	96.3	112.1	92.5	95.2	101.0	103.0	107.4	98.1	166.8	19.67
65.98	28.81	-13.52	202.41	.68	5.10	.46	97.6	114.7	92.9	96.4	103.6	105.3	110.2	100.5	170.8	19.61
71.29	28.78	-13.60	201.97	.79	5.12	.39	99.2	117.7	93.6	98.2	106.8	108.3	113.6	103.5	175.4	19.59
76.45	28.77	-13.69	202.18	.98	5.00	.35	100.9	120.8	94.3	100.1	110.1	111.3	117.2	106.6	179.7	19.61
81.01	↓	-13.74	201.69	1.09	5.09	.31	102.4	123.4	94.9	102.0	113.0	113.9	120.4	109.5	183.4	19.61
86.47		-13.85	201.61	1.23	5.01	.31	104.3	126.8	95.9	104.5	116.7	117.3	124.2	113.2	187.8	19.63
91.02		-13.92	201.92	1.32	4.80	.19	105.9	129.4	96.6	106.5	119.8	120.1	127.4	116.2	191.4	19.64
96.43	28.79	-14.05	201.80	1.37	4.96	.18	107.8	132.6	97.5	109.0	123.4	123.4	131.1	119.8	195.4	19.69
101.04	28.73	-14.04	201.43	1.51	4.89	.17	109.8	135.4	98.4	111.2	126.6	126.3	134.4	123.1	198.8	19.63
106.51	28.76	-14.06	201.51	1.64	4.89	.18	112.1	138.7	99.5	113.7	130.4	129.9	138.3	127.0	202.5	19.61
111.01	28.77	-14.16	201.57	1.67	4.74	.13	113.9	141.4	100.5	116.0	133.5	132.8	141.6	130.2	205.6	19.64
116.32	28.71	-14.19	201.43	1.94	4.72	.09	116.2	144.5	101.6	118.4	137.1	136.2	145.2	134.0	209.0	19.63
121.48	28.71	-14.23	201.36	1.99	4.62	.15	118.3	147.4	102.6	120.7	140.6	139.4	148.7	137.6	212.2	19.61
133.36	-.07	-1.39	.38	1.68	-.45	-.21	123.7	151.8	105.2	125.2	149.2	145.9	151.9	145.5	210.2	3.37

Table III. Continued

Δt_{time}	F_N	F_A	M_Y	M_X	M_Z	F_Y	T_2	T_3	T_4	T_5	T_6	T_7	T_8	T_{ij}	p_{ij}
Powered configuration; Ar-Fr exhaust gas; $M_\infty = 5.81$; $R_\infty = 0.59 \times 10^6/\text{ft}$; $\alpha = -0.03^\circ$; T_1 not reporting															
0	0.08	-0.03	0.29	0.46	-0.82	0.18	79.8	80.2	79.7	78.0	79.6	78.9	77.9	77.4	0.08
39.98	4.18	-22.96	29.28	.55	3.15	-.47	82.0	80.5	79.9	78.2	80.1	79.8	78.0	105.8	18.90
45.24	4.01	-22.68	30.04	.69	3.19	-.51	83.9	80.6	80.1	78.3	80.7	80.5	78.1	113.7	18.54
50.65	4.33	-25.02	32.78	.92	3.42	-.53	86.2	80.9	80.4	78.7	81.8	81.5	78.5	121.4	20.42
55.46	4.16	-24.58	32.69	1.15	3.46	-.51	88.5	81.1	80.7	79.3	83.0	82.7	79.1	127.2	20.07
60.47	3.90	-23.07	31.27	1.34	3.33	-.49	90.8	81.4	81.1	80.0	84.4	84.0	79.9	131.9	18.80
64.98	3.92	-23.21	31.54	1.32	3.31	-.52	93.1	81.8	81.6	80.9	85.9	85.4	80.7	136.0	18.73
69.54	4.18	-25.00	33.48	1.51	3.56	-.57	95.4	82.4	82.3	82.0	87.5	87.4	81.8	140.6	20.23
74.95	4.16	-24.68	33.02	1.67	3.44	-.52	98.3	83.2	83.1	83.6	89.6	89.7	83.3	145.6	19.94
80.01	4.07	-23.90	31.87	1.71	3.27	-.50	101.0	84.0	84.1	85.2	91.8	91.9	84.8	149.8	19.38
85.42	4.02	-23.31	31.01	1.87	3.24	-.50	103.9	85.0	85.3	87.2	94.1	94.4	86.7	154.1	18.77
89.58	4.24	-24.61	32.24	1.91	3.30	-.54	106.1	85.7	86.1	88.7	96.0	96.3	88.2	157.6	19.47
94.64	4.34	-25.14	32.63	2.12	3.33	-.52	108.8	86.8	87.3	90.6	98.4	98.9	90.1	162.0	20.14
100.10	4.28	-24.83	32.28	2.14	3.31	-.47	111.8	88.0	88.6	92.8	101.1	101.7	92.4	166.3	19.85
105.41	4.14	-23.94	31.15	2.41	3.31	-.44	114.8	89.3	89.9	95.1	103.8	104.5	94.6	170.2	19.19
110.42	4.09	-23.53	30.65	2.41	3.29	-.48	117.6	90.6	91.4	97.3	106.4	107.0	97.0	173.8	18.75
115.32	4.41	-25.32	32.33	2.49	3.41	-.49	120.4	92.0	92.9	99.6	109.1	109.6	99.3	177.7	19.88
135.36	.17	-1.01	.35	.56	-.42	.09	123.6	96.9	96.7	109.2	116.1	114.8	107.5	157.3	1.40
Powered configuration; Ar-Fr exhaust gas; $M_\infty = 5.79$; $R_\infty = 0.60 \times 10^6/\text{ft}$; $\alpha = 5.09^\circ$; T_1 not reporting															
0	0.11	-0.01	0.33	0.49	-0.60	0.16	83.6	83.2	82.7	80.8	82.9	82.1	80.7	80.2	0.11
25.35	5.94	-23.36	37.51	-.07	2.95	-.45	83.7	83.7	83.1	81.0	83.3	82.4	80.8	92.7	12.93
35.32	5.76	-22.97	37.07	.79	3.33	-.61	88.3	83.9	83.4	81.1	84.2	84.7	81.3	151.5	19.21
40.18	5.73	-22.57	36.35	1.11	3.43	-.66	92.1	84.2	83.6	81.4	85.4	86.3	81.7	165.1	18.65
45.74	6.10	-24.78	38.28	1.42	3.75	-.75	97.0	84.7	84.0	82.2	87.8	89.1	82.7	178.2	20.11
49.90	6.06	-24.74	38.17	1.68	3.77	-.76	100.9	85.2	84.6	83.2	90.1	91.8	83.8	186.0	20.22
54.91	6.00	-24.43	37.70	1.92	3.75	-.74	105.6	85.9	85.4	84.9	93.3	95.1	85.4	193.2	19.93
60.92	5.81	-23.22	36.34	2.26	3.74	-.73	111.3	87.0	86.4	87.5	97.2	99.3	87.9	199.6	18.82
65.33	5.60	-22.88	34.95	2.36	3.67	-.71	115.4	88.1	87.6	89.9	100.4	102.6	90.2	203.6	18.52
70.39	5.94	-25.27	37.24	2.63	3.88	-.73	119.9	89.6	89.1	93.0	104.5	106.7	93.2	209.1	20.24
75.60	5.88	-24.97	36.86	2.86	3.90	-.73	124.5	91.4	90.7	96.4	108.6	111.0	96.4	213.6	20.04
81.21	5.82	-24.60	36.28	3.06	3.90	-.73	129.3	93.4	92.5	100.2	112.9	115.2	100.1	217.8	19.67
86.07	5.77	-24.27	35.85	3.20	3.91	-.73	133.3	95.3	94.4	103.7	116.6	119.1	103.5	221.1	19.36
90.18	5.70	-24.00	35.55	3.40	3.86	-.70	136.6	97.0	95.9	106.7	119.9	122.2	106.4	223.6	19.10
95.13	5.64	-23.67	35.14	3.46	3.79	-.66	140.4	99.1	98.0	110.3	123.6	126.1	110.0	226.5	18.79
105.20	.12	-1.04	.47	2.57	-.41	.03	144.1	102.5	101.4	118.3	128.8	127.3	116.3	205.7	3.09

Table III. Concluded

Δt_{ime}	F_N	F_A	M_Y	M_X	M_Z	F_Y	T_2	T_3	T_4	T_5	T_6	T_7	T_8	T_{ij}	p_{ij}
Powered configuration; Ar-Fr exhaust gas; $M_\infty = 6.02$; $R_\infty = 7.26 \times 10^6/\text{ft}$; $\alpha = 0.04^\circ$; T_1 not reporting															
0	0.17	0.02	0.45	0.41	0.26	-0.09	90.3	89.2	88.2	84.4	87.6	86.7	83.5	83.2	0.36
28.00	8.21	-13.98	104.61	1.27	2.75	1.14	99.5	90.6	89.4	86.3	91.1	93.2	85.3	184.4	17.82
34.27	8.79	-17.47	107.47	1.80	2.84	1.19	104.8	91.6	90.1	88.5	94.2	97.4	86.8	199.6	20.48
39.48	8.72	-17.13	107.01	2.05	2.91	1.23	109.8	92.7	90.9	91.3	97.4	101.4	88.9	208.1	20.17
43.58	8.57	-16.44	105.93	2.38	2.84	1.19	113.7	93.7	91.8	94.0	100.2	104.8	90.9	213.3	19.68
48.54	8.40	-15.28	104.49	2.44	2.84	1.20	118.4	95.1	93.0	97.6	103.7	108.7	93.8	218.0	18.53
53.70	8.70	-16.85	105.81	2.79	2.83	1.20	123.1	97.0	94.7	101.9	107.9	113.4	97.3	223.3	19.18
59.12	8.88	-18.19	106.55	2.99	2.88	1.23	128.2	99.6	97.0	106.7	112.7	119.4	101.5	229.3	20.51
63.77	8.78	-17.74	106.22	3.10	2.99	1.28	132.6	101.8	99.1	111.1	116.7	124.1	105.4	233.2	20.14
68.48	8.54	-16.43	104.73	3.38	2.99	1.28	136.8	104.0	101.4	115.7	121.0	128.7	109.6	236.5	19.25
73.04	8.38	-15.59	103.69	3.35	2.96	1.27	140.6	106.3	103.5	120.1	124.8	132.9	113.6	239.0	18.33
78.45	8.76	-18.09	105.59	3.58	2.82	1.20	145.0	109.2	106.3	125.3	129.6	138.3	118.7	243.0	19.75
83.16	8.85	-18.55	106.11	3.71	3.00	1.30	148.8	112.0	109.0	129.9	134.0	143.5	123.2	246.5	20.41
88.12	8.73	-18.05	105.63	3.96	2.89	1.24	152.7	114.8	111.8	134.7	138.3	148.2	128.0	249.5	19.98
93.23	8.64	-17.53	104.94	4.07	2.91	1.25	156.7	117.7	114.7	139.5	142.8	152.8	132.9	252.3	19.50
98.04	8.54	-17.00	104.51	4.05	2.88	1.24	160.2	120.4	117.5	144.0	146.8	157.0	137.6	254.6	19.08
103.15	8.45	-16.52	103.64	4.16	3.80	1.13	163.8	123.3	120.7	148.7	151.2	161.4	142.5	257.0	18.63
108.46	8.93	-18.90	105.91	4.36	2.90	1.25	167.6	126.3	124.1	153.5	155.9	166.5	147.6	260.3	20.30
113.57	8.84	-18.53	105.25	4.38	2.67	1.13	171.2	129.3	127.2	158.0	160.0	171.3	152.5	263.0	20.07
120.53	-0.06	-1.79	.86	4.14	.21	-0.09	174.3	132.0	130.6	164.4	163.8	171.0	158.4	251.1	5.02
124.94	.01	-1.78	1.02	2.66	.01	-0.16	173.3	134.1	132.9	168.2	166.5	172.0	162.0	245.3	2.70
147.58	.03	-1.67	.93	1.54	-0.54	-0.27	167.8	145.4	144.8	181.7	174.5	180.2	177.3	221.7	3.58
152.94	.01	-1.61	1.03	1.64	-0.61	-0.31	167.0	147.3	146.9	183.7	175.5	181.5	179.9	220.2	3.61
Powered configuration; Ar-Fr exhaust gas; $M_\infty = 6.03$; $R_\infty = 7.28 \times 10^6/\text{ft}$; $\alpha = 4.79^\circ$; T_1 not reporting															
0	0.11	-0.02	0.28	0.41	0.37	-0.08	101.8	104.1	103.2	97.5	99.1	98.0	94.9	94.4	0.40
36.42	28.41	-9.32	179.82	.39	3.25	1.25	109.8	105.9	104.5	100.3	102.1	105.2	96.8	198.6	16.49
52.30	29.24	-14.64	183.72	1.33	3.68	1.48	122.5	109.4	107.3	108.2	111.3	117.0	103.1	231.1	20.27
56.56	29.07	-13.92	183.00	1.50	3.77	1.53	126.2	110.7	108.5	111.3	114.3	120.5	105.7	236.0	19.65
60.37	28.80	-12.73	181.54	1.73	3.57	1.42	129.4	112.1	109.6	114.3	117.1	123.7	108.2	239.5	18.71
65.28	28.64	-12.03	180.65	2.00	3.63	1.46	133.4	113.8	111.3	118.5	120.9	127.7	111.8	243.5	18.01
69.73	29.08	-14.53	182.66	2.07	3.68	1.48	136.9	115.8	113.0	122.5	124.6	131.6	115.4	247.9	19.27
75.34	29.26	-16.19	183.79	2.25	3.75	1.52	141.4	118.8	115.8	127.9	129.7	137.5	120.4	254.1	21.01
80.25	29.05	-15.20	182.66	2.62	3.72	1.51	145.4	121.4	118.5	132.7	134.3	142.5	125.1	258.0	20.23
85.46	28.82	-14.17	181.48	2.89	3.58	1.44	149.4	124.0	121.2	137.8	138.9	147.1	130.0	261.3	19.36
90.22	28.66	-13.26	180.56	3.07	3.60	1.45	153.0	126.5	123.8	142.5	142.9	151.5	134.6	264.1	18.59
95.68	28.91	-14.91	181.77	3.16	3.64	1.47	157.0	129.6	126.7	147.9	147.6	156.6	139.9	267.7	19.51
101.04	28.97	-15.58	181.96	3.37	3.71	1.51	160.8	132.8	129.8	153.1	152.4	161.8	145.1	271.4	20.16
105.20	28.87	-15.19	181.32	3.71	3.46	1.39	163.8	135.3	132.4	157.1	156.0	165.7	149.2	273.8	19.85
110.06	28.77	-14.81	180.75	3.73	3.43	1.37	167.2	138.1	135.3	161.8	160.2	170.2	154.0	276.5	19.49
115.12	28.79	-14.76	181.01	3.87	3.41	1.36	170.6	141.1	138.3	166.5	164.4	174.6	158.9	279.1	19.37
119.98	28.79	-14.82	180.55	3.89	3.54	1.43	173.9	143.8	141.2	170.9	168.4	178.7	163.5	281.4	19.38
124.24	28.83	-14.94	180.85	4.00	3.45	1.39	176.6	146.2	143.7	174.7	171.8	182.4	167.4	283.5	19.41
138.42	-0.08	-1.50	1.11	2.71	.44	-0.21	181.2	153.0	151.4	187.5	180.0	184.8	179.4	264.6	2.53

Table IV. Balance 2042 Zero Shifts

$R_{\infty}, \text{ft}^{-1}$	α, deg	Zero shift, percent of full scale		
		F_A	M_Y	F_N
Unpowered configuration				
0.63×10^6	-3.45	-2.4	0	0
$.63 \times 10^6$	-.04	0.7	.1	↓
$.57 \times 10^6$	5.00	-0.9	0	↓
1.18×10^6	-.08	2.7	0	↓
2.10×10^6	-3.47	-4.0	0	-1
2.09×10^6	-.05	-1.7	-1	0
2.12×10^6	4.89	1.1	0	-1
4.04×10^6	-0.16	2.7	↓	0
7.47×10^6	-3.49	-3.9	↓	0
7.40×10^6	-.15	10.4	↓	-.2
7.43×10^6	5.09	3.1	↓	0
Powered configuration; jet off				
0.56×10^6	-0.18	0.1	0	0
$.57 \times 10^6$	4.90	-1.4	0	0
7.35×10^6	-.04	-2.8	.1	-1
7.45×10^6	5.06	-2.4	-.2	0
Powered configuration; cold air				
0.61×10^6	-0.12	1.8	0	0
$.60 \times 10^6$	4.99	-1.5	0	-1
7.32×10^6	.08	-1.7	0	-.2
7.36×10^6	5.22	3.4	-.5	.2
Powered configuration; hot air				
0.61×10^6	-0.07	-3.0	0	-3
$.60 \times 10^6$	5.03	-3.5	0	0
7.39×10^6	.06	-4.9	.2	-.2
7.38×10^6	5.01	-7.0	0	-.2
Powered configuration; Ar-Fr				
0.59×10^6	-0.03	-4.9	0	.1
$.60 \times 10^6$	5.09	-5.2	.1	0
7.26×10^6	.04	-8.0	.3	-.2
7.29×10^6	4.79	-7.4	.4	-.2

Table V. Balance 2042 Wind-On Shifts in F_A

R_∞, ft^{-1}	α, deg	Run time, sec	Shift, percent of full scale
Unpowered			
0.63×10^6	-3.45	74	-0.5
$.63 \times 10^6$	-.04	80	-.3
$.57 \times 10^6$	5.00	84	-.4
1.18×10^6	-.08	78	-.5
2.10×10^6	-3.47	85	-1.2
2.09×10^6	-.05	35	-1.4
2.12×10^6	4.89	81	-.8
4.04×10^6	-.16	111	-.3
7.47×10^6	-3.49	110	-1.8
7.40×10^6	-.15	107	-4.2
7.43×10^6	5.09	111	-2.8
Powered; jet off			
0.55×10^6	-0.18	55	-0.5
$.57 \times 10^6$	4.90	90	-.4
7.35×10^6	-.04	81	(a)
7.45×10^6	5.06	70	(a)
Powered; cold air			
0.61×10^6	-0.12	86	(b)
$.60 \times 10^6$	4.99	80	(b)
7.32×10^6	.08	79	(b)
7.36×10^6	5.22	85	(b)
Powered; hot air			
0.61×10^6	-0.07	90	(b)
$.60 \times 10^6$	5.03	90	(b)
7.39×10^6	.06	90	(b)
7.38×10^6	5.01	110	(b)
Powered; Ar-Fr			
0.59×10^6	-0.03	92	(b)
$.60 \times 10^6$	5.09	70	(b)
7.26×10^6	.04	85	(b)
7.29×10^6	4.79	88	(b)

^aProblems with data acquisition preclude reporting wind-on axial-force shift for these runs.

^bAxial-force shifts during jet-on powered runs could not be established because of oscillations.

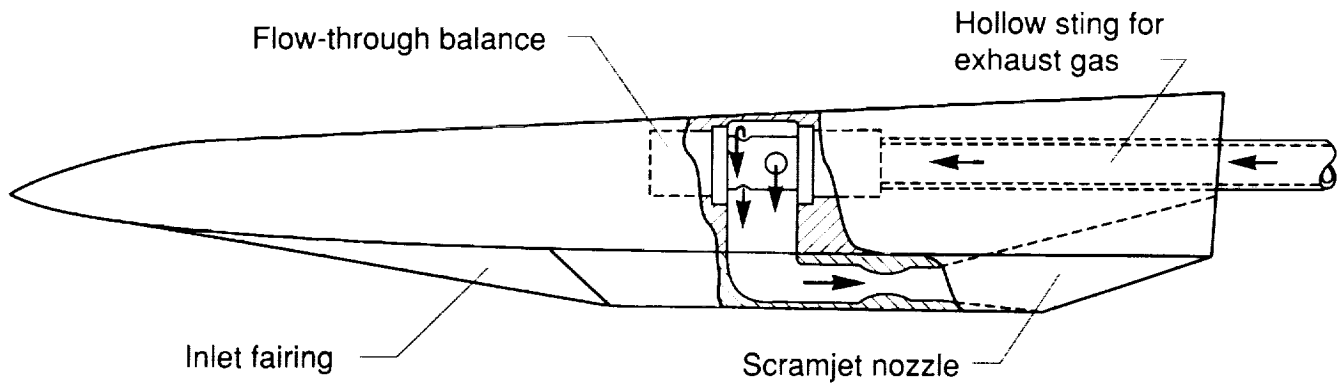


Figure 1. Simulant gas flow path for HAPCM-50 powered configuration with flow-through balance.

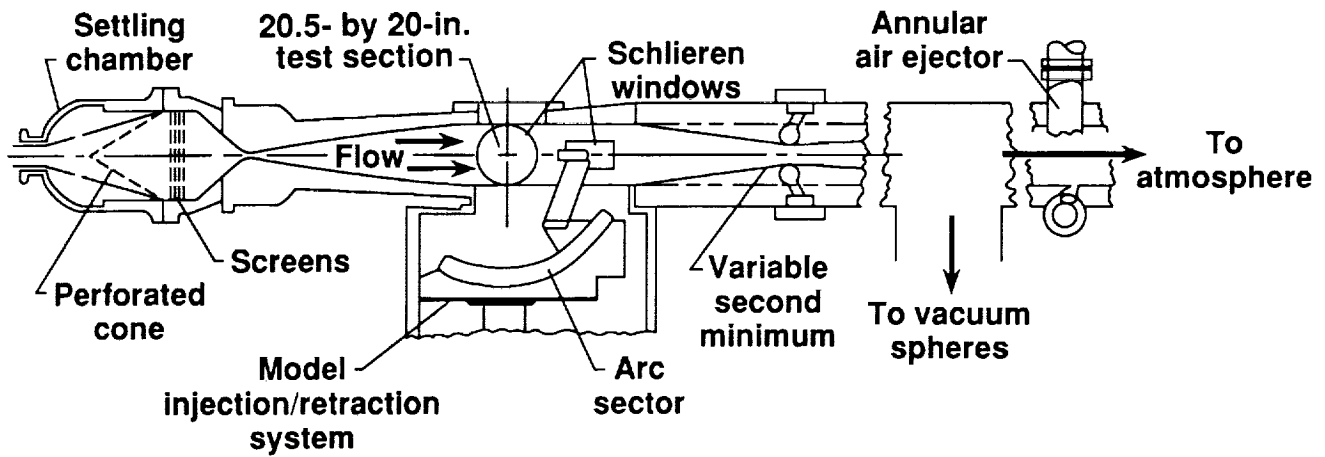


Figure 2. Schematic of 20-Inch Mach 6 Wind Tunnel.

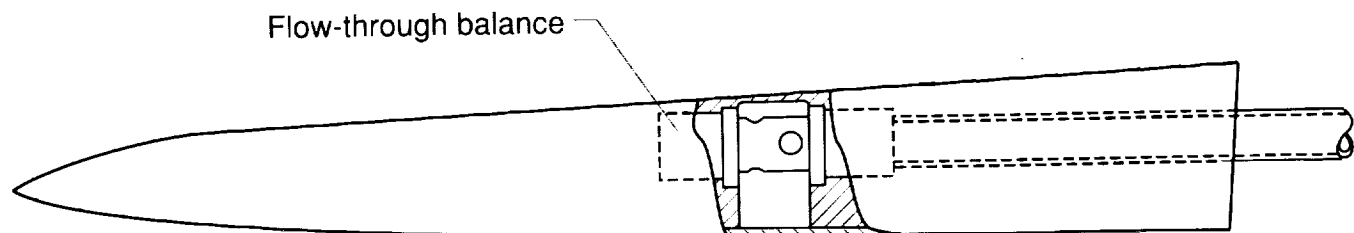


Figure 3. HAPCM-50 unpowered configuration with flow-through balance.

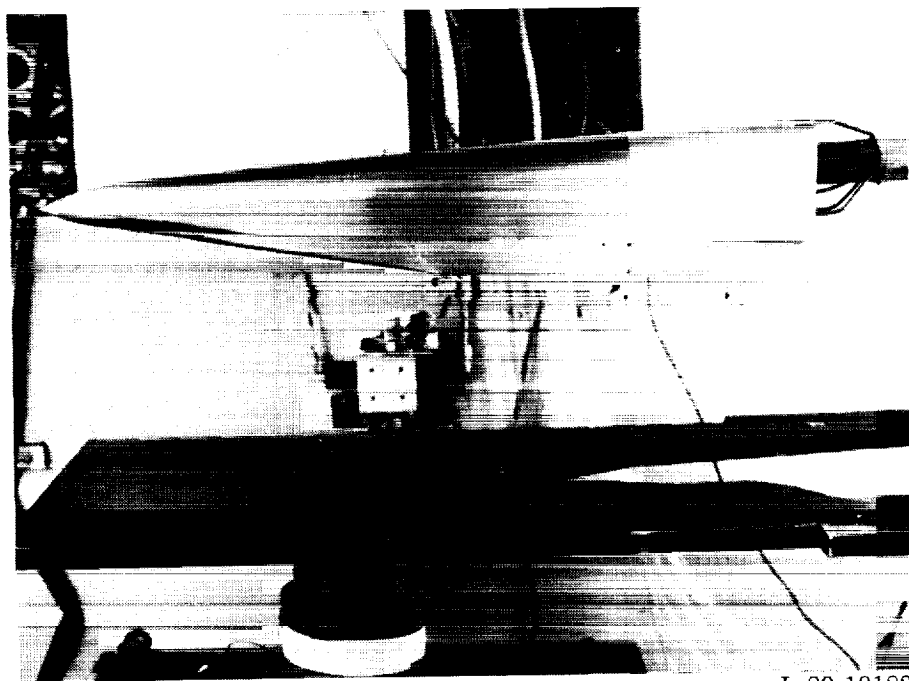
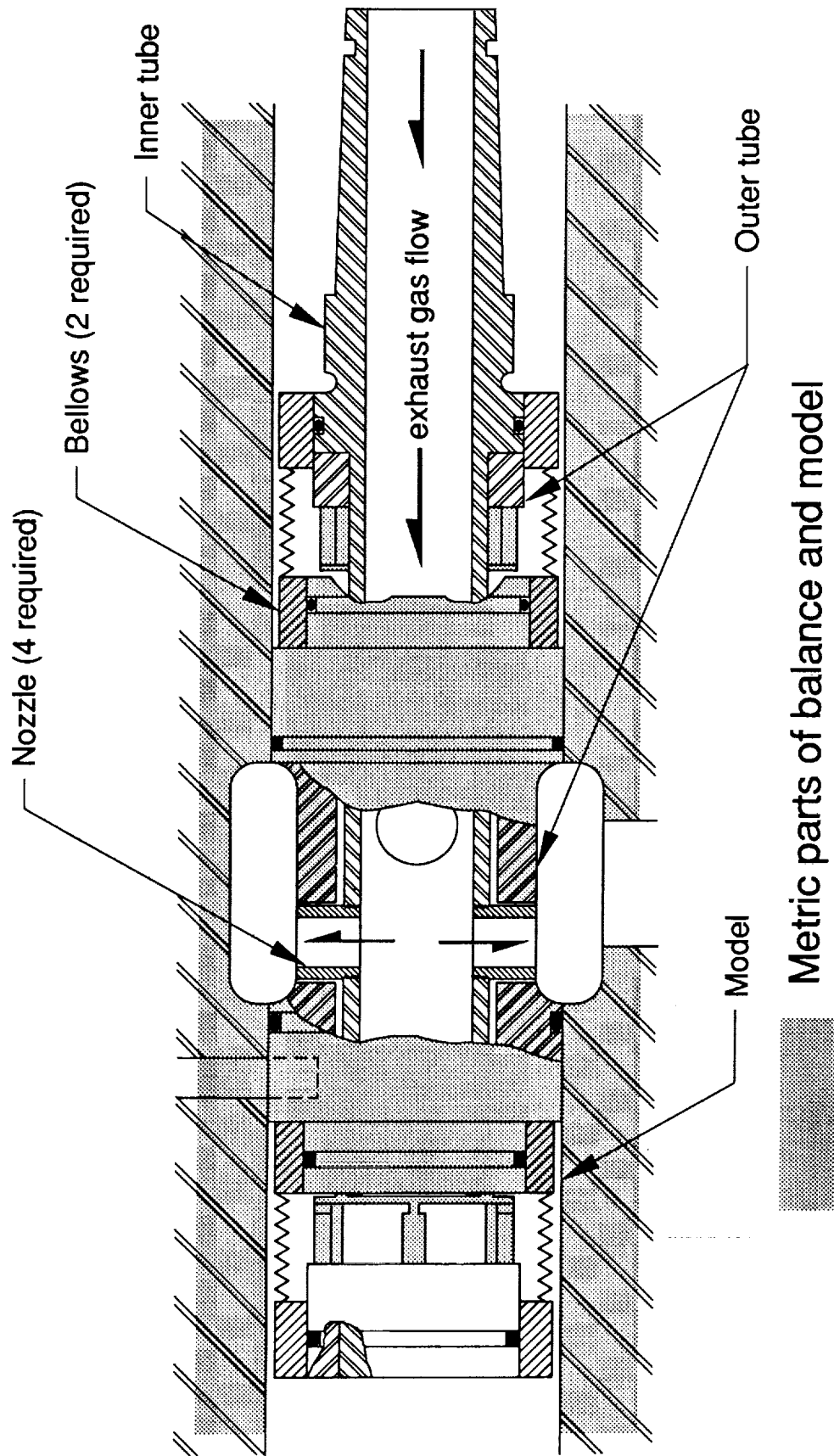


Figure 4. HAPCM-50 powered configuration in 20-Inch Mach 6 Wind Tunnel.

ORIGINAL PAGE
BLACK AND WHITE PHOTOGRAPH



Metric parts of balance and model

Figure 5. Balance 2042 assembly drawing.

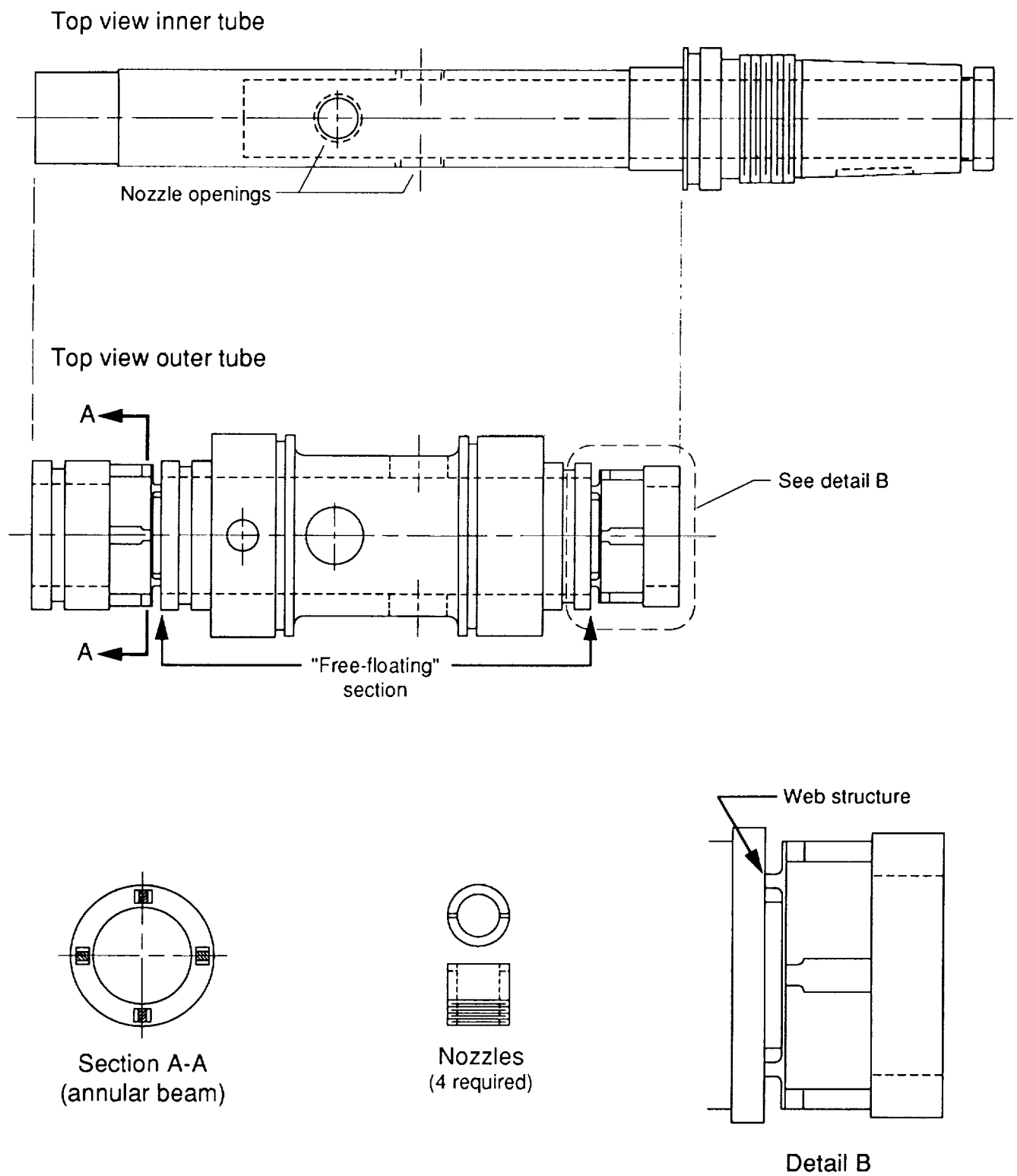


Figure 6. Details of balance 2042.

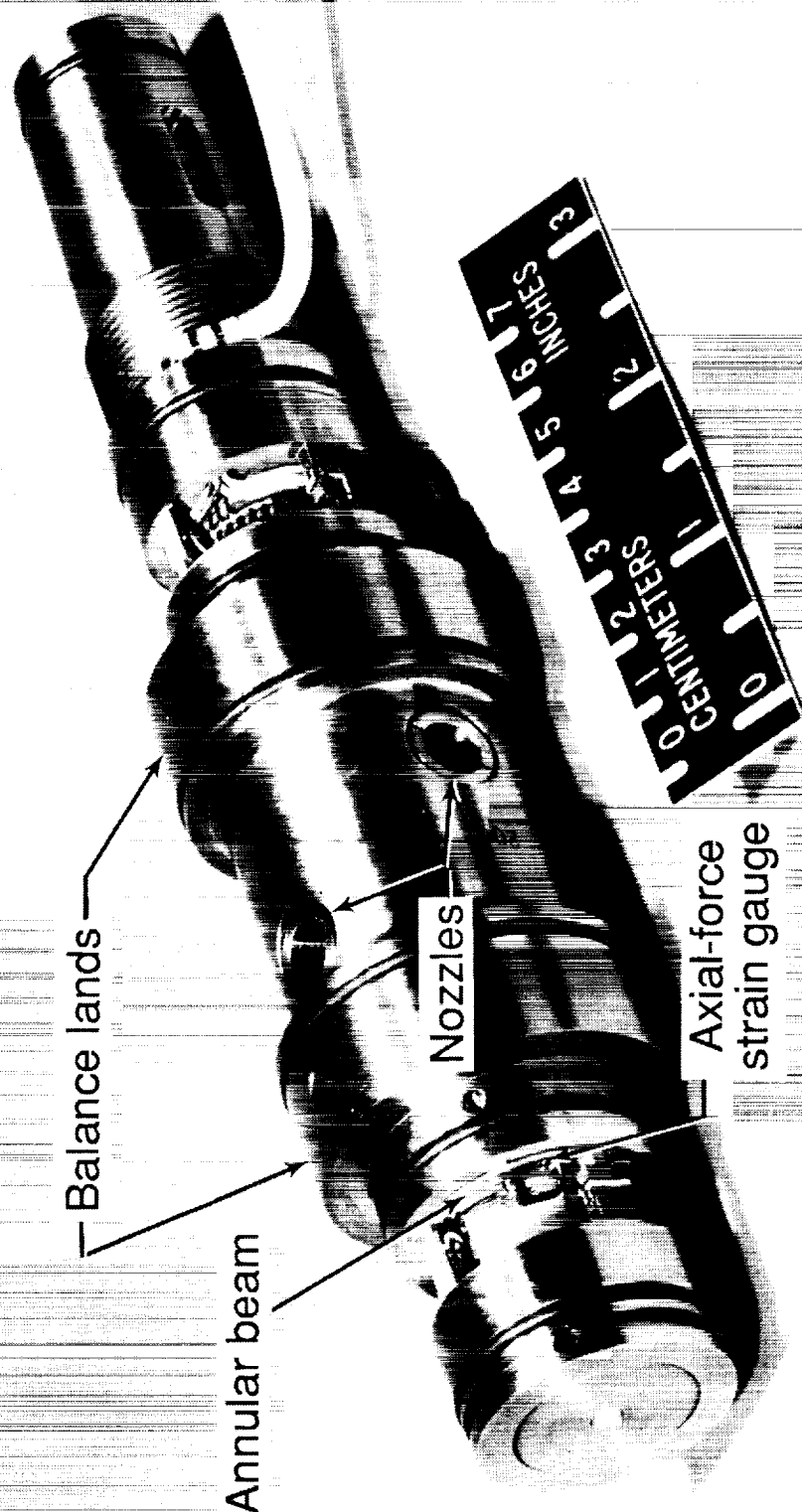
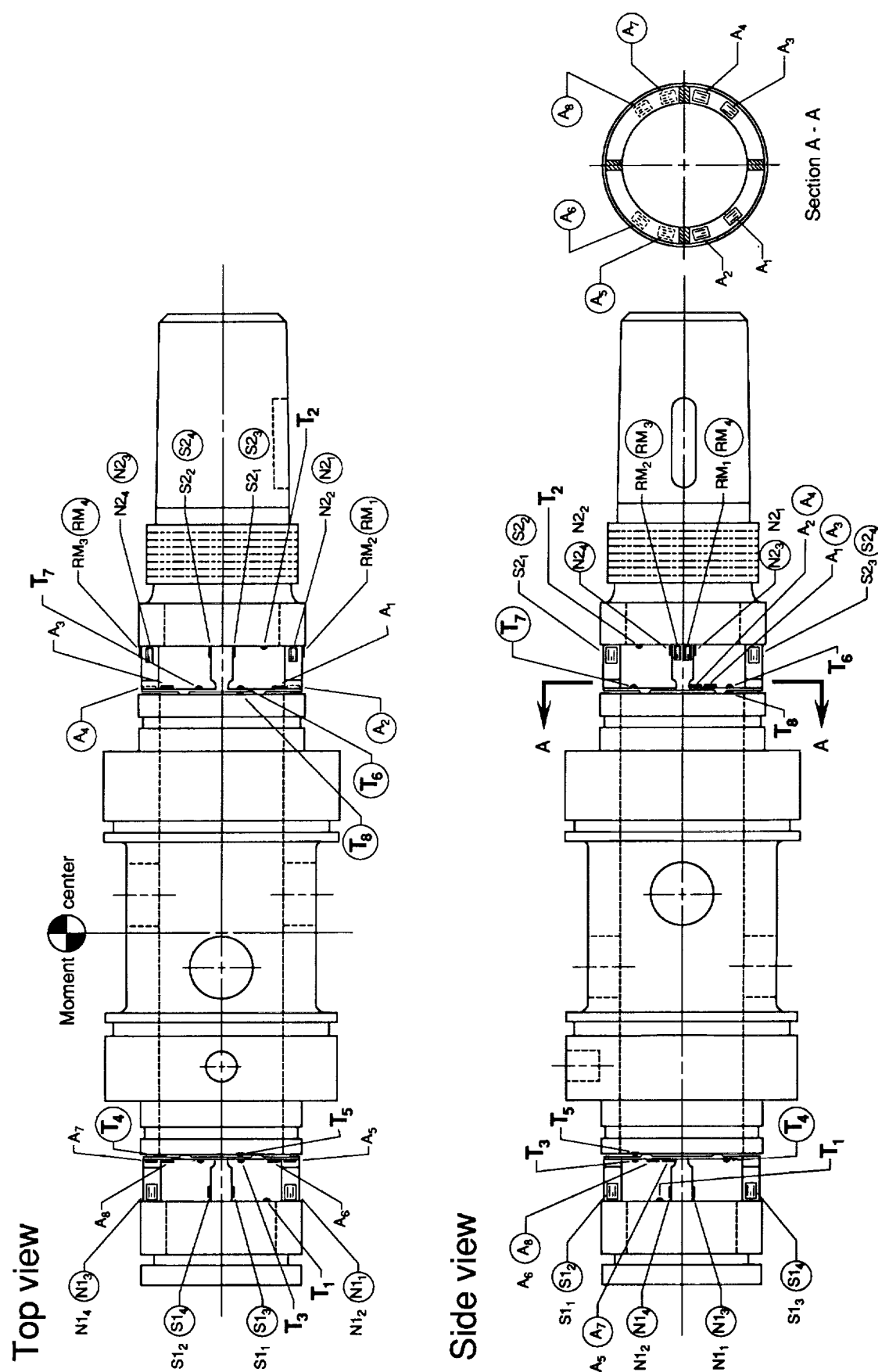
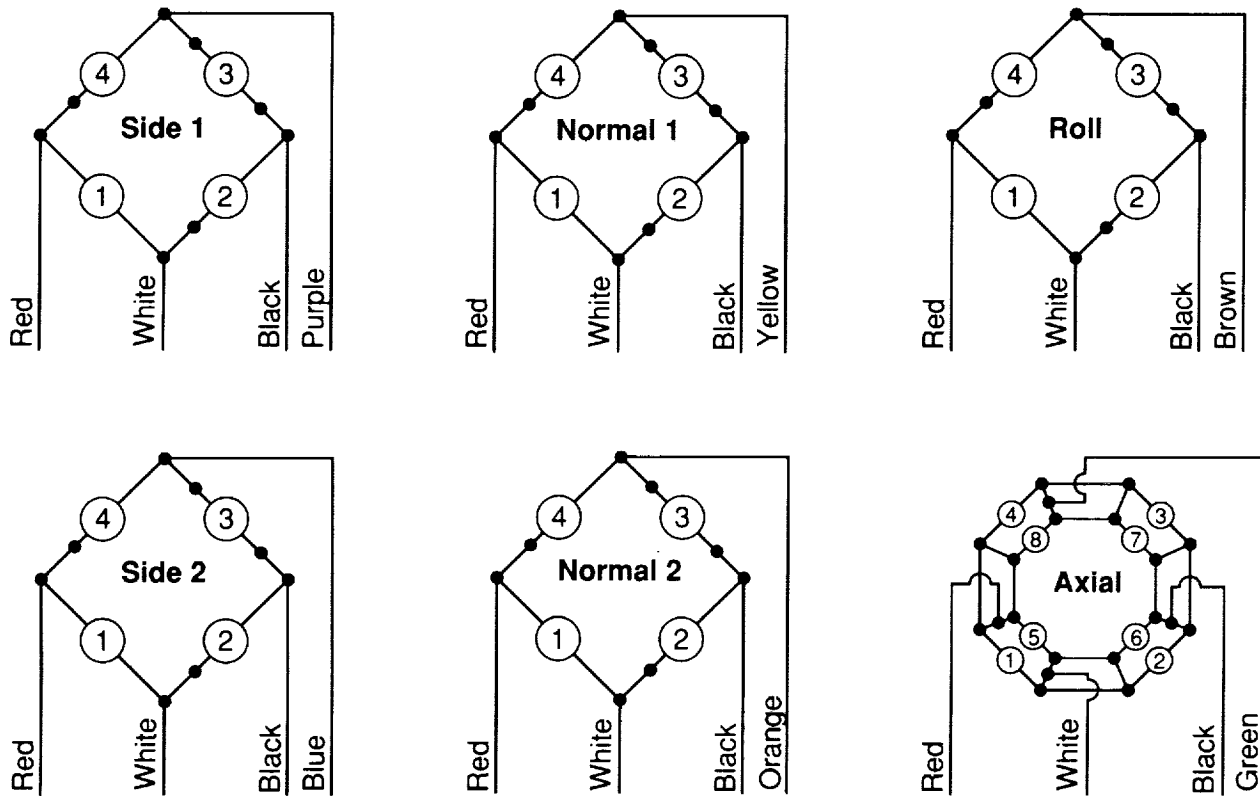


Figure 7. Annular beams and axial strain gauge on balance 2042.



(a) Strain gauge and thermocouple locations.

Figure 8. Balance 2042 strain gauge circuit and thermocouple information. Circles denote gauges and thermocouples on opposite end or side of balance.



(b) Wheatstone bridge strain gauge circuit diagrams.

Figure 8. Concluded.

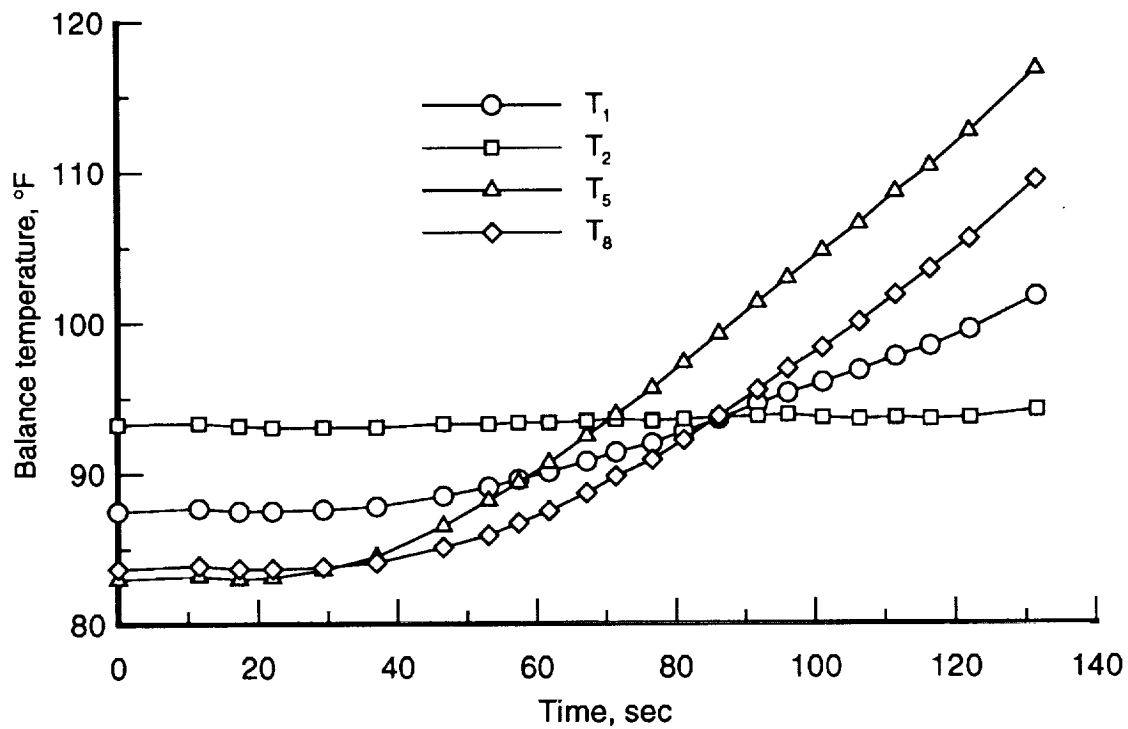


Figure 9. Balance temperature time histories, unpowered configuration. $M_\infty = 6.01$; $R_\infty = 7.43 \times 10^6/\text{ft}$; $\alpha = 5.09^\circ$.

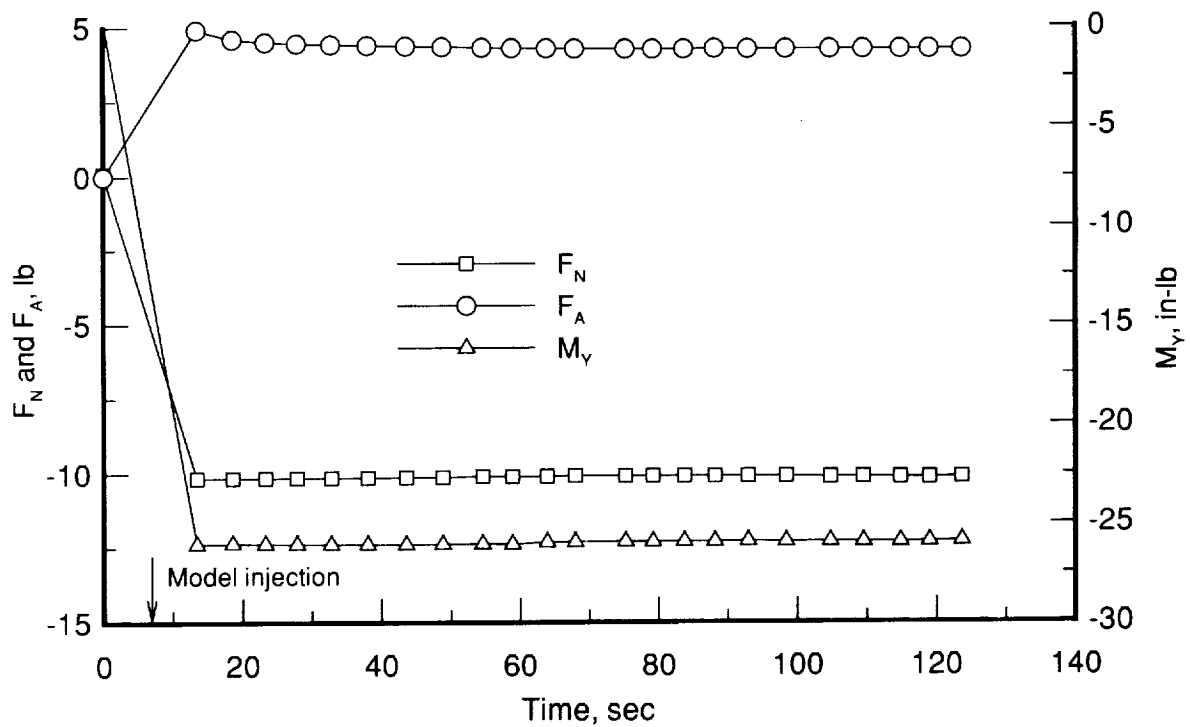


Figure 10. Force and moment time histories, unpowered configuration. $M_\infty = 6.01$; $R_\infty = 7.47 \times 10^6/\text{ft}$; $\alpha = -3.49^\circ$.

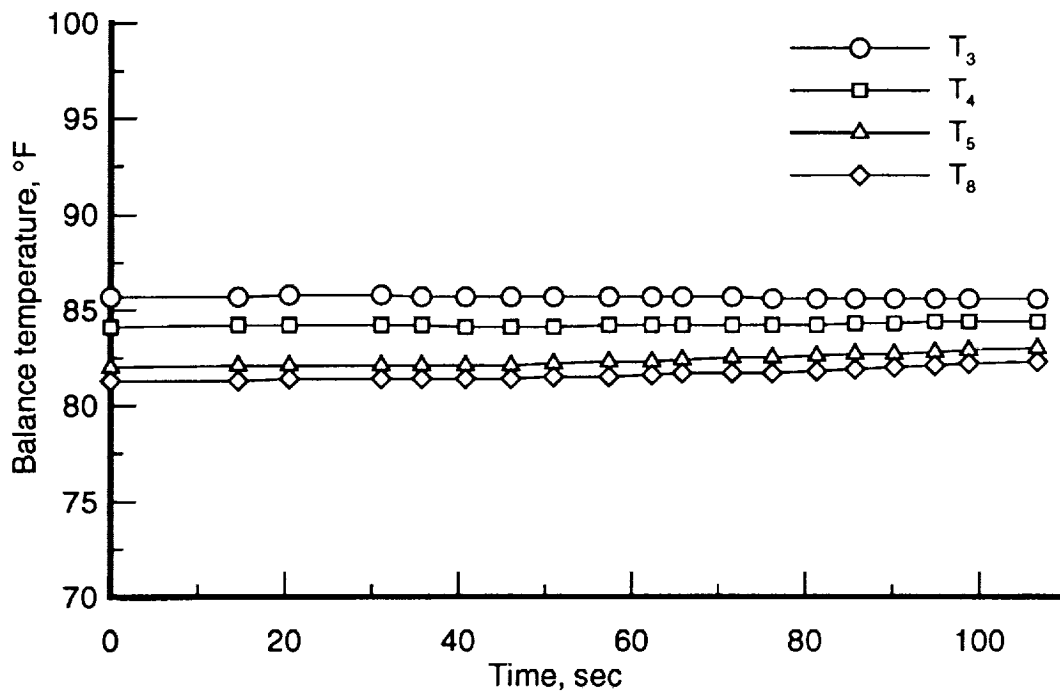


Figure 11. Balance temperature time histories, unpowered configuration. $M_\infty = 5.79$; $R_\infty = 0.57 \times 10^6/\text{ft}$; $\alpha = 5.00^\circ$.

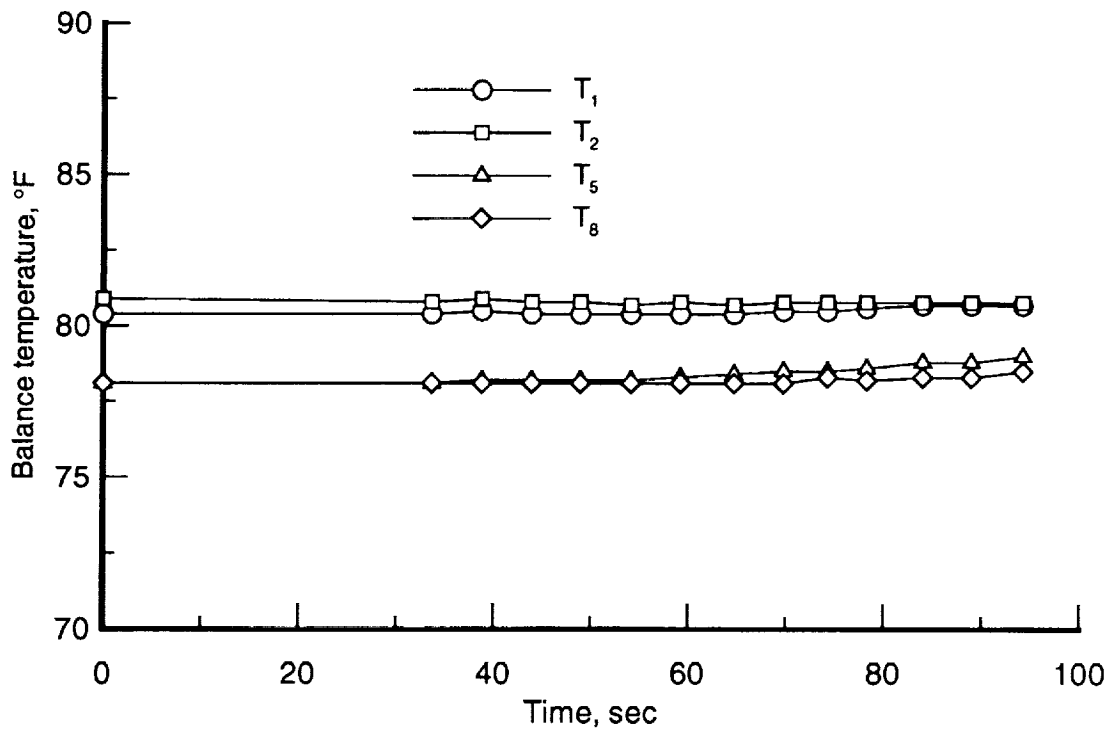


Figure 12. Balance temperature time histories, powered configuration, no exhaust flow. $M_\infty = 5.82$; $R_\infty = 0.56 \times 10^6/\text{ft}$; $\alpha = -0.18^\circ$.

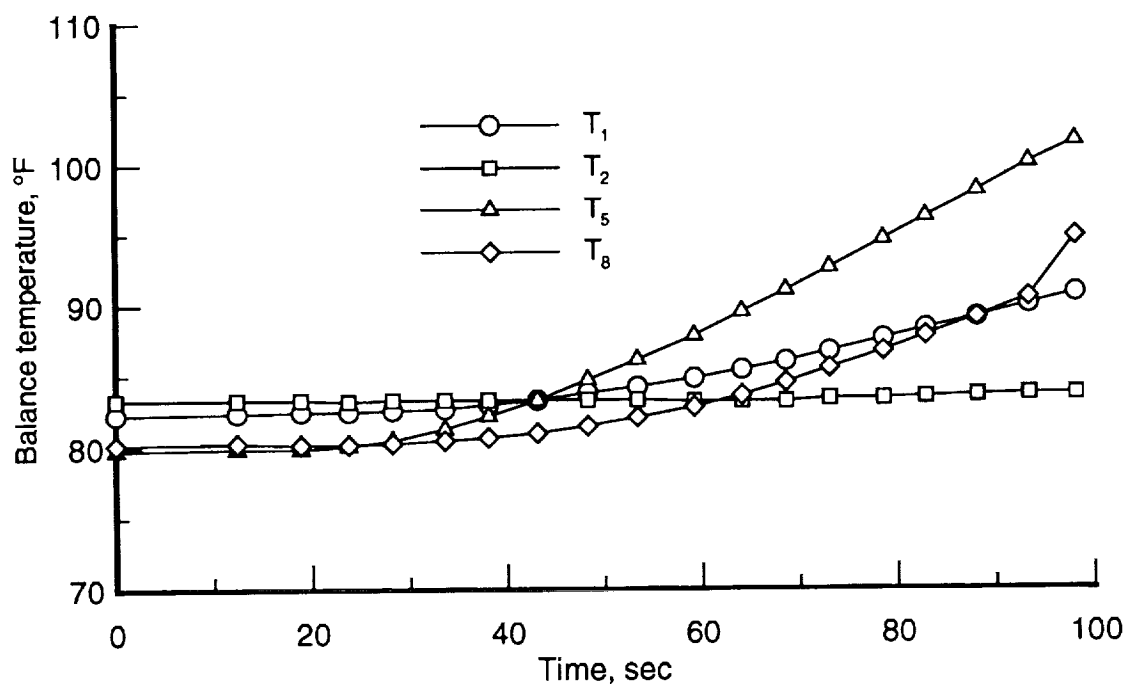


Figure 13. Balance temperature time histories, powered configuration, no exhaust flow. $M_\infty = 6.02$; $R_\infty = 7.35 \times 10^6/\text{ft}$; $\alpha = -0.04^\circ$.

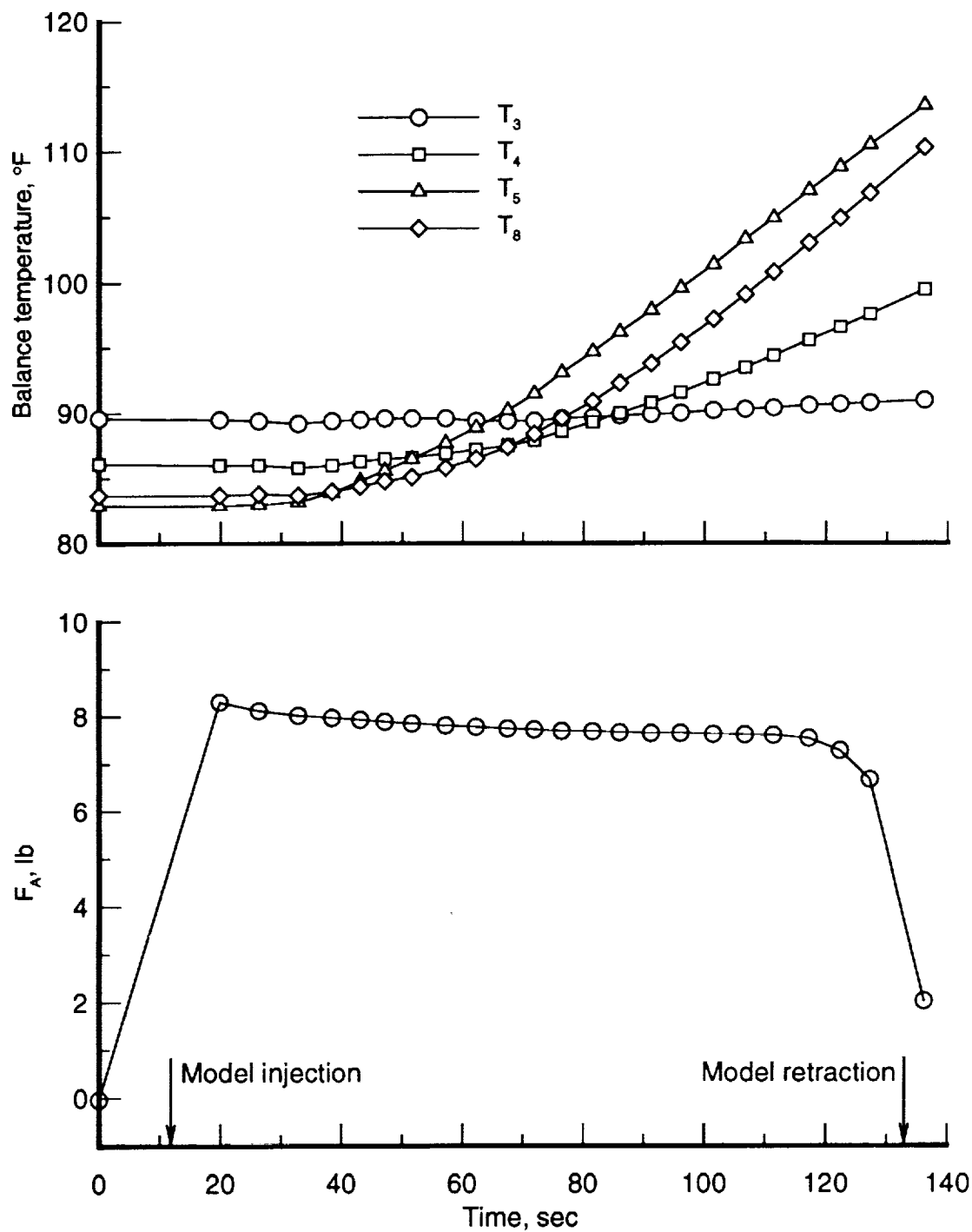


Figure 14. Axial-force and balance temperature time histories, unpowered configuration. $M_\infty = 6.02$; $R_\infty = 7.40 \times 10^6/\text{ft}$; $\alpha = -0.15^\circ$.

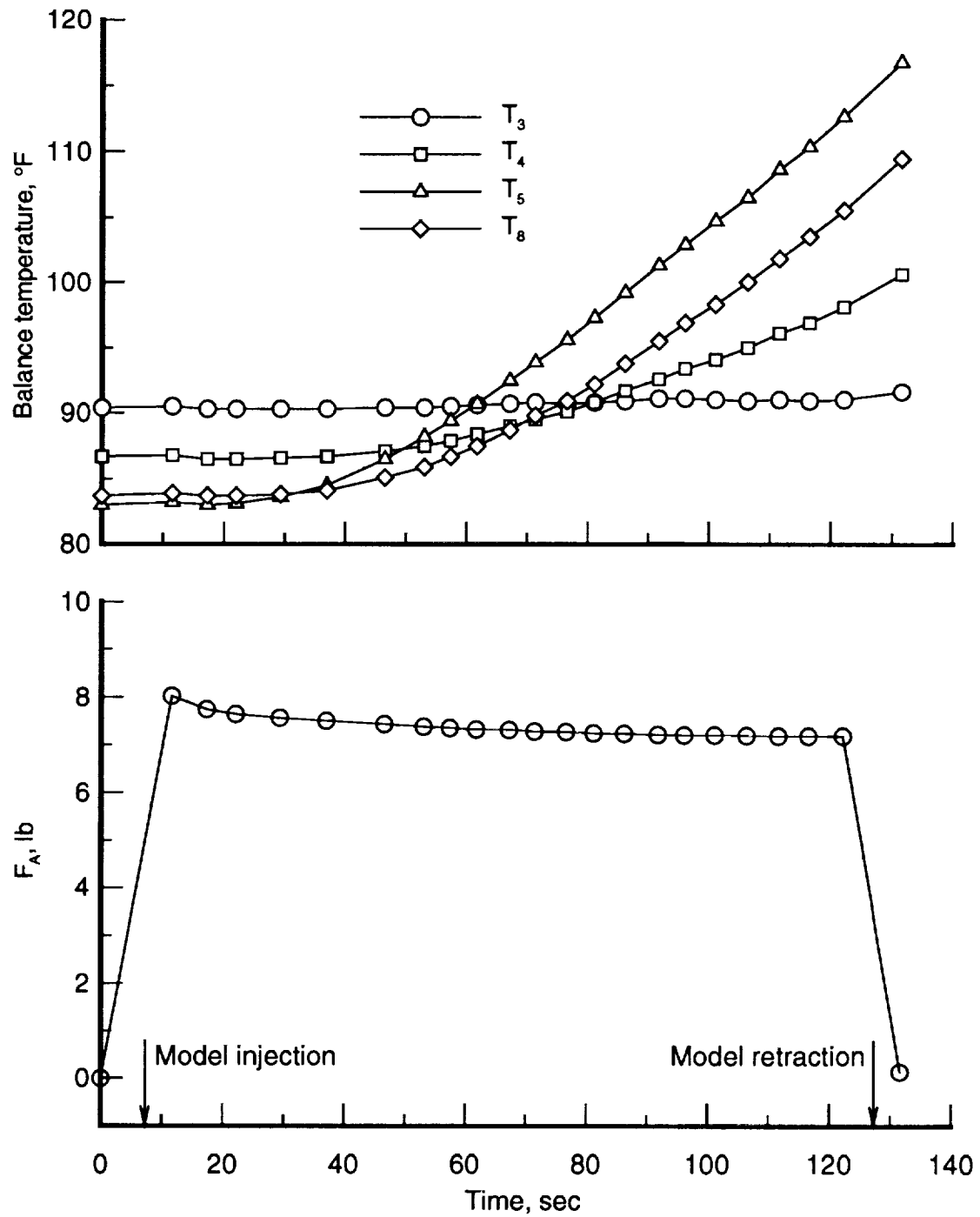


Figure 15. Axial-force and temperature time histories, unpowered configuration. $M_\infty = 6.01$; $R_\infty = 7.43 \times 10^6/\text{ft}$; $\alpha = 5.09^\circ$.

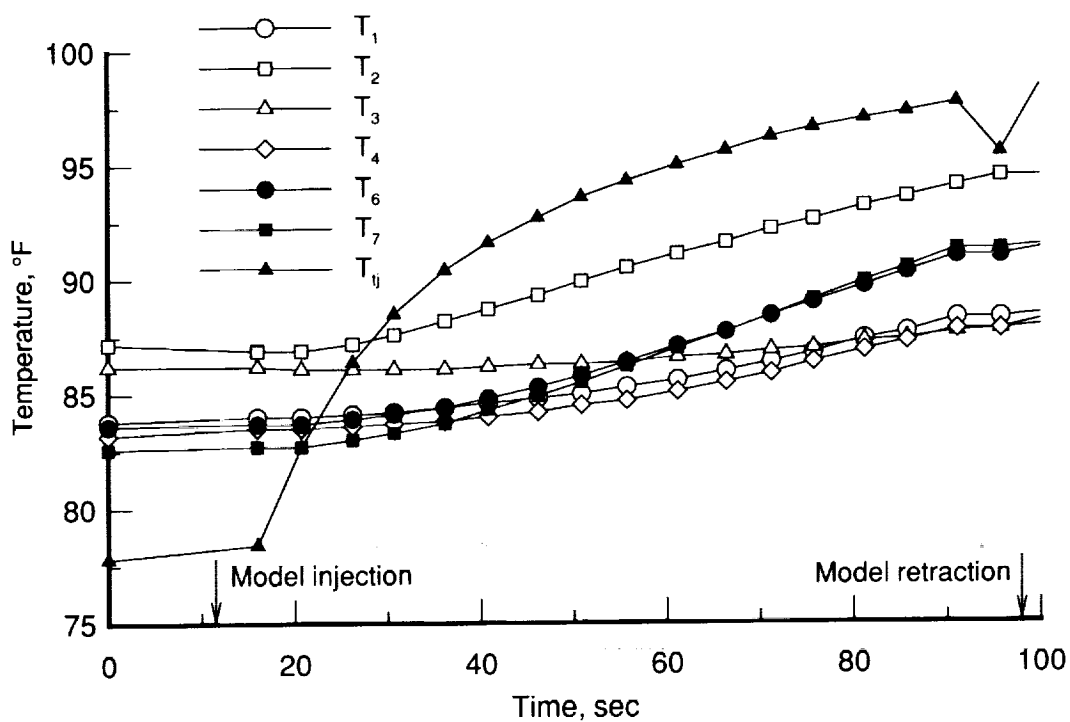


Figure 16. Temperature time histories, powered configuration, cold air. $M_\infty = 5.79$; $R_\infty = 0.60 \times 10^6/\text{ft}$; $\alpha = 4.99^\circ$.

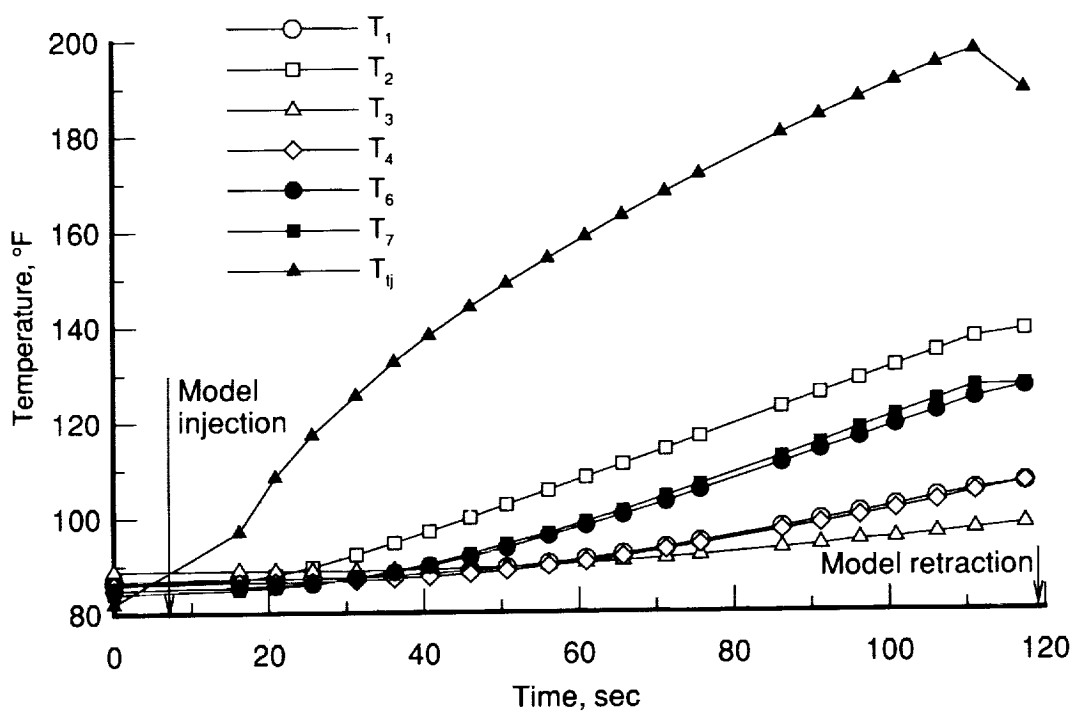


Figure 17. Temperature time histories, powered configuration, hot air. $M_\infty = 5.79$; $R_\infty = 0.60 \times 10^6/\text{ft}$; $\alpha = 5.03^\circ$.

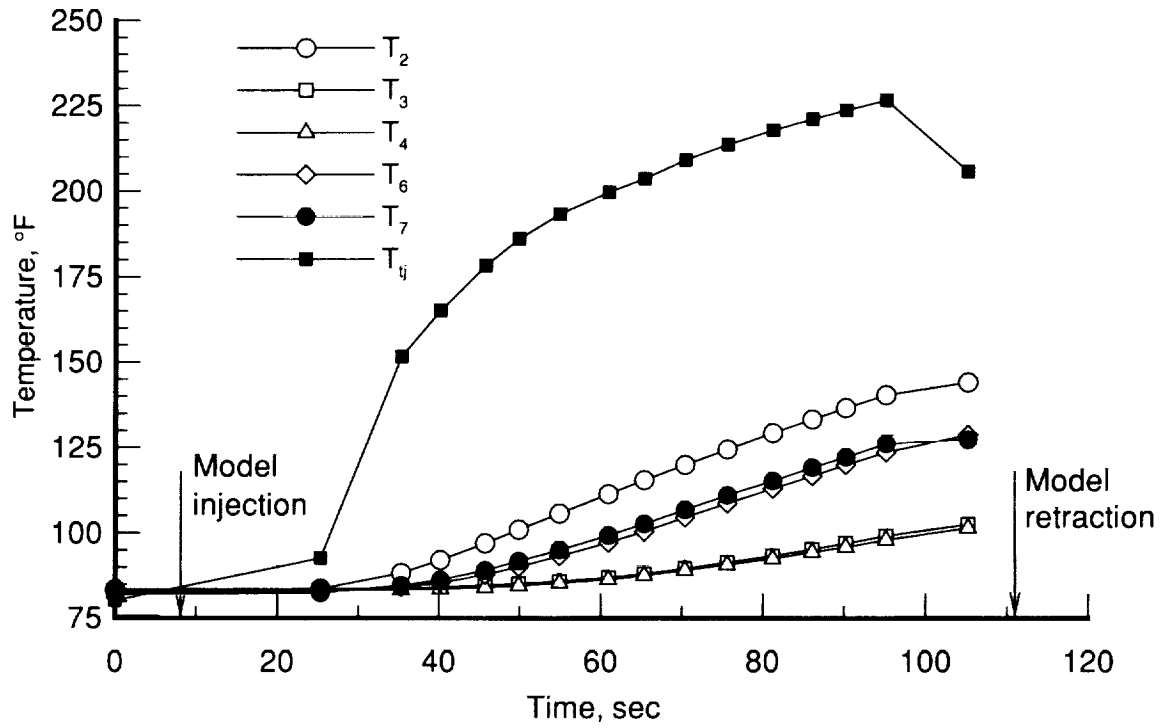


Figure 18. Temperature time histories, powered configuration, Ar-Fr. $M_\infty = 5.79$; $R_\infty = 0.60 \times 10^6/\text{ft}$; $\alpha = 5.09^\circ$.

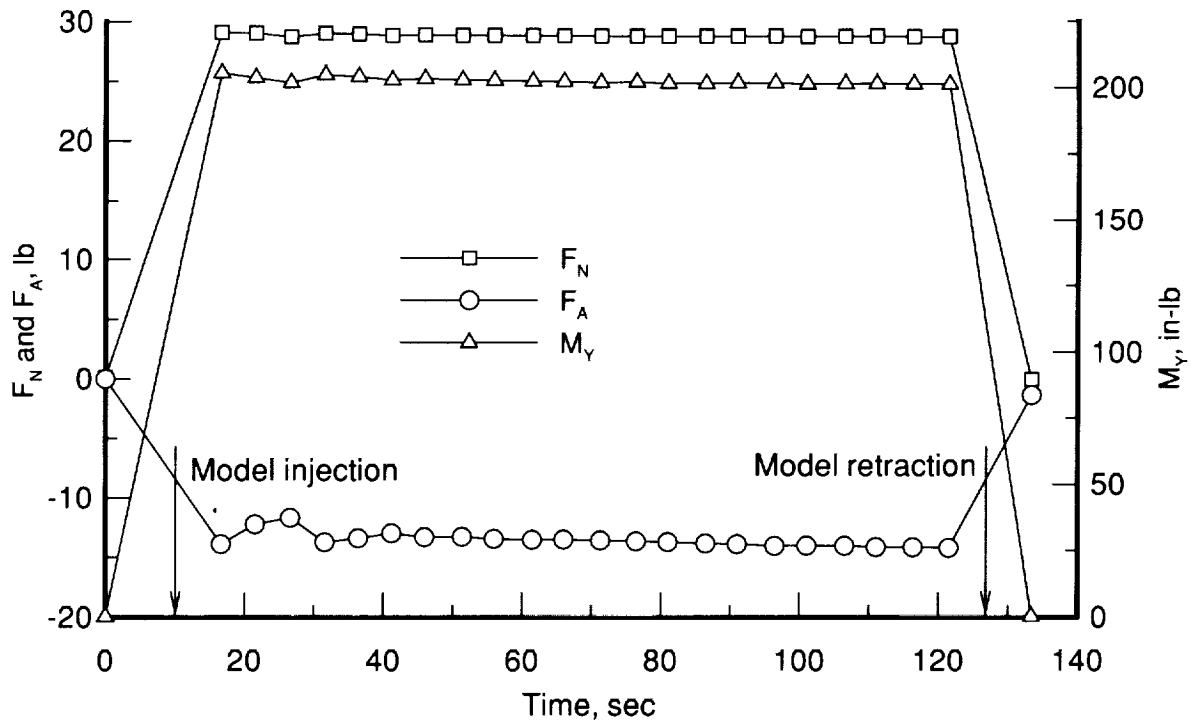


Figure 19. Force and moment time histories, powered configuration, hot air. $M_\infty = 6.01$; $R_\infty = 7.38 \times 10^6/\text{ft}$; $\alpha = 5.01^\circ$.

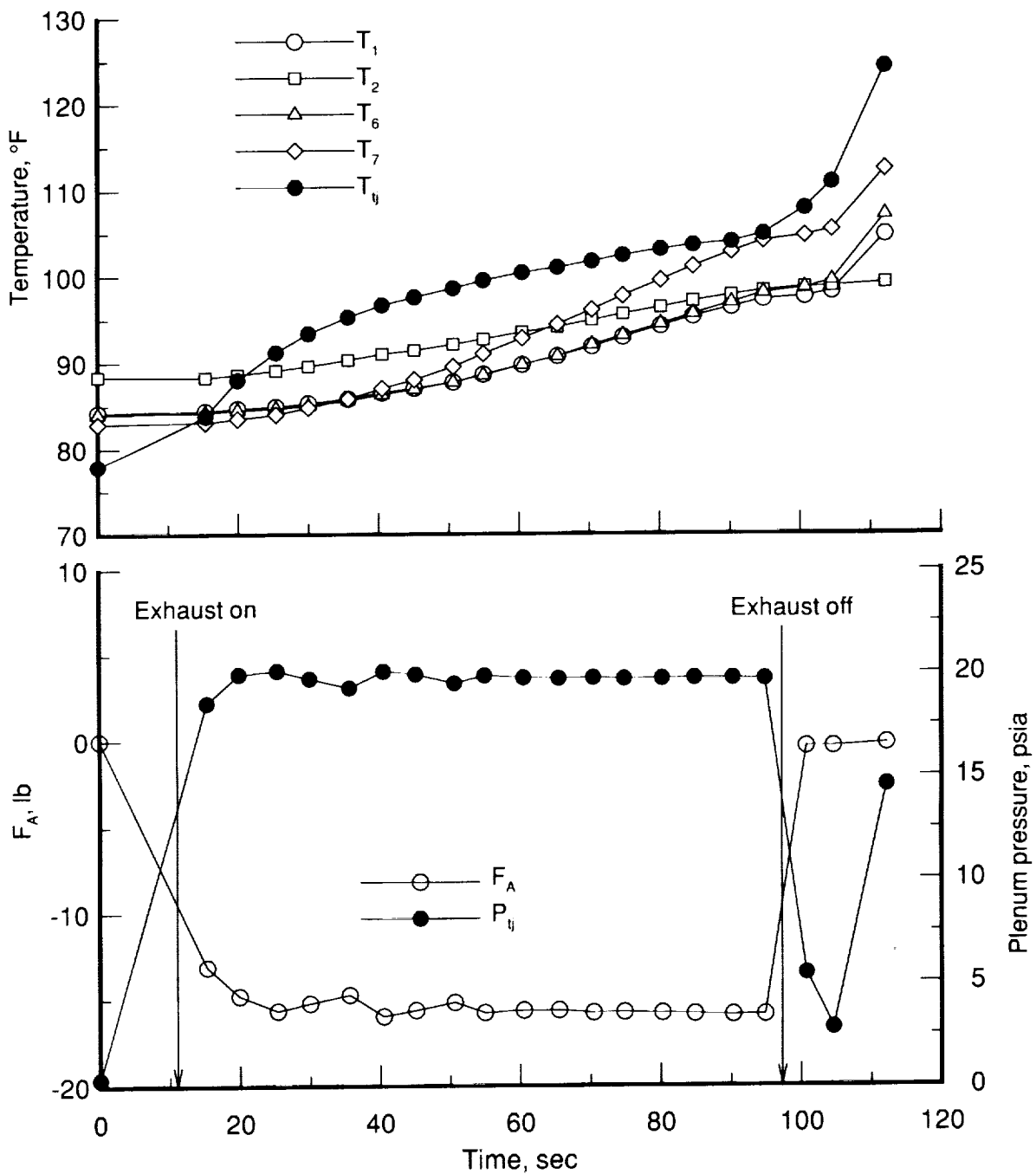


Figure 20. Axial-force and balance temperature time histories, powered configuration, cold air. $M_\infty = 6.02$; $R_\infty = 7.32 \times 10^6/\text{ft}$; $\alpha = 0.08^\circ$.

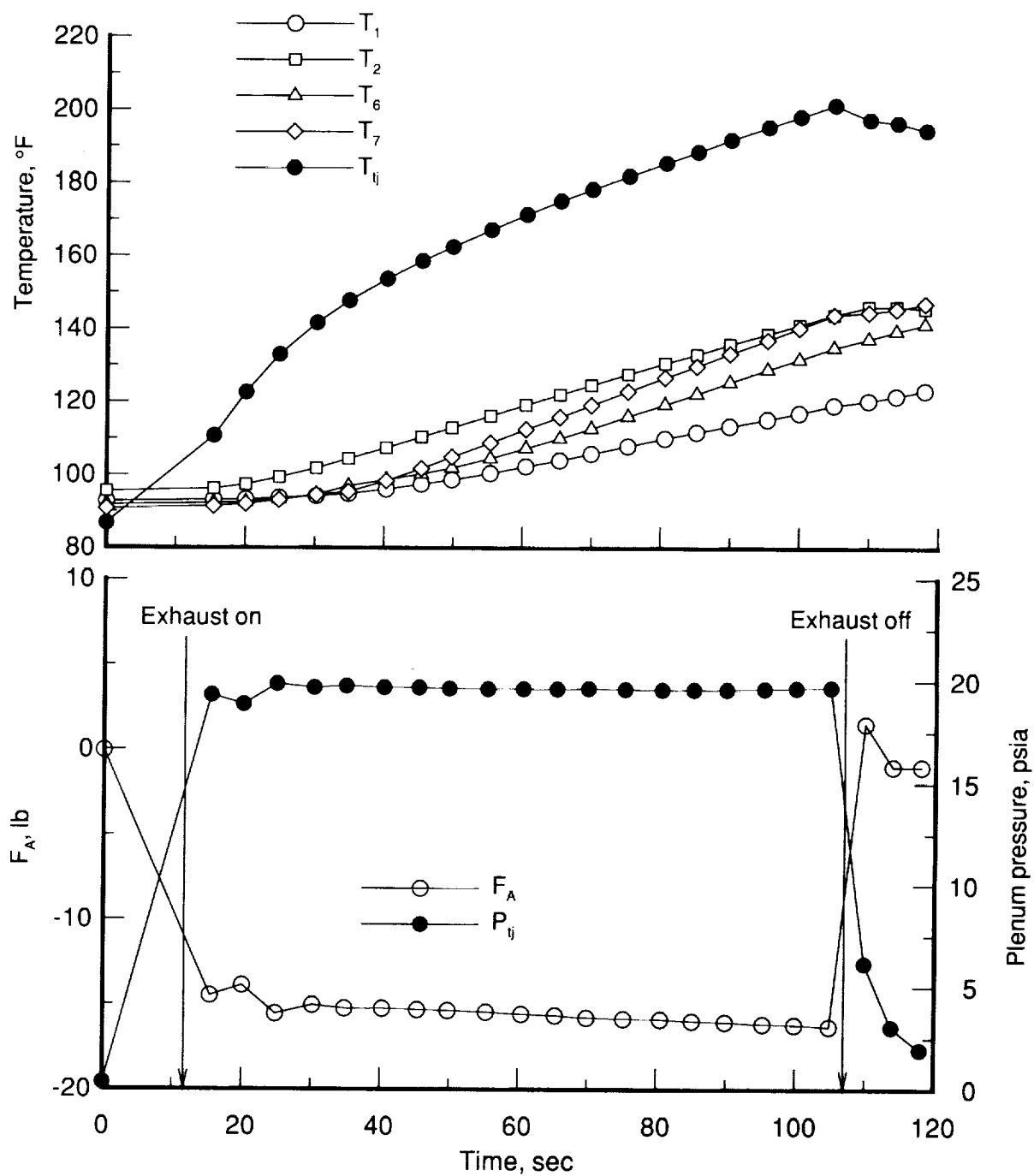


Figure 21. Axial-force and balance temperature time histories, powered configuration, hot air. $M_\infty = 6.01$; $R_\infty = 7.39 \times 10^6/\text{ft}$; $\alpha = 0.06^\circ$.

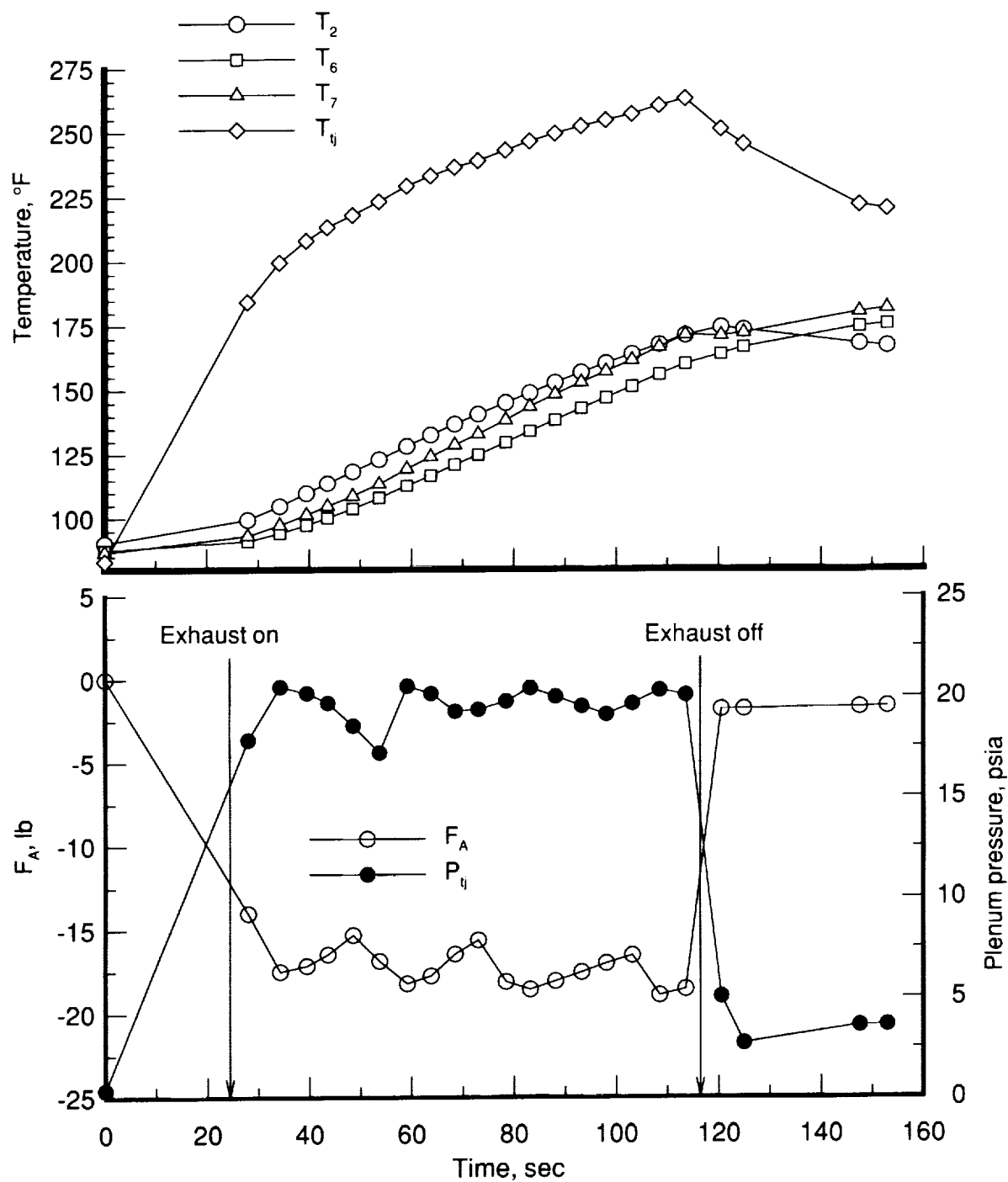


Figure 22. Axial-force and balance temperature time histories, powered configuration, Ar-Fr. $M_\infty = 6.02$; $R_\infty = 7.26 \times 10^6/\text{ft}$; $\alpha = 0.04^\circ$.

REPORT DOCUMENTATION PAGE			Form Approved OMB No. 0704-0188	
Public reporting burden for this collection of information is estimated to average 1 hour per response, including the time for reviewing instructions, searching existing data sources, gathering and maintaining the data needed, and completing and reviewing the collection of information. Send comments regarding this burden estimate or any other aspect of this collection of information, including suggestions for reducing this burden, to Washington Headquarters Services, Directorate for Information Operations and Reports, 1215 Jefferson Davis Highway, Suite 1204, Arlington, VA 22202-4302, and to the Office of Management and Budget, Paperwork Reduction Project (0704-0188), Washington, DC 20503.				
1. AGENCY USE ONLY (Leave blank)		2. REPORT DATE May 1993		3. REPORT TYPE AND DATES COVERED Technical Memorandum
4. TITLE AND SUBTITLE Assessment of a Flow-Through Balance for Hypersonic Wind Tunnel Models With Scramjet Exhaust Flow Simulation			5. FUNDING NUMBERS WU 505-59-40-03	
6. AUTHOR(S) Lawrence D. Huebner, Marc W. Kniskern, and William J. Monta				
7. PERFORMING ORGANIZATION NAME(S) AND ADDRESS(ES) NASA Langley Research Center Hampton, VA 23681-0001			8. PERFORMING ORGANIZATION REPORT NUMBER L-17088	
9. SPONSORING/MONITORING AGENCY NAME(S) AND ADDRESS(ES) National Aeronautics and Space Administration Washington, DC 20546-0001			10. SPONSORING/MONITORING AGENCY REPORT NUMBER NASA TM-4441	
11. SUPPLEMENTARY NOTES Huebner and Monta: Langley Research Center, Hampton, VA; Kniskern: North Carolina State University, Raleigh, NC.				
12a. DISTRIBUTION/AVAILABILITY STATEMENT Unclassified-Unlimited Subject Category 02			12b. DISTRIBUTION CODE	
13. ABSTRACT (Maximum 200 words) The purposes of this investigation were twofold: first, to determine whether accurate force and moment data could be obtained during hypersonic wind tunnel tests of a model with a scramjet exhaust flow simulation that uses a representative nonwatercooled, flow-through balance; second, to analyze temperature time histories on various parts of the balance to address thermal effects on force and moment data. The tests were conducted in the NASA Langley Research Center 20-Inch Mach 6 Wind Tunnel at free-stream Reynolds numbers ranging from 0.5 to $7.4 \times 10^6/\text{ft}$ and nominal angles of attack of -3.5° , 0° , and 5° . The simulant exhaust gases were cold air, hot air, and a mixture of 50 percent Argon and 50 percent Freon by volume, which reached stagnation temperatures within the balance of 111° , 214° , and 283°F , respectively. All force and moment values were unaffected by the balance thermal response from exhaust gas simulation and external aerodynamic heating except for axial-force measurements, which were significantly affected by balance heating. This investigation showed that for this model at the conditions tested, a nonwatercooled, flow-through balance is not suitable for axial-force measurements during scramjet exhaust flow simulation tests at hypersonic speeds. In general, heated exhaust gas may produce unacceptable force and moment uncertainties when used with thermally sensitive balances.				
14. SUBJECT TERMS Flow-through balance; Scramjet exhaust flow simulation; Hypersonic aerodynamics; Thermal effects			15. NUMBER OF PAGES 47	
			16. PRICE CODE A03	
17. SECURITY CLASSIFICATION OF REPORT Unclassified	18. SECURITY CLASSIFICATION OF THIS PAGE Unclassified	19. SECURITY CLASSIFICATION OF ABSTRACT	20. LIMITATION OF ABSTRACT	

NSN 7540-01-280-5500

Standard Form 298 (Rev. 2-89)
Prescribed by ANSI Std. Z39-18
298-102

NASA-Langley, 1993